The Astrophysical Journal, 885:166 (18pp), 2019 November 10 https://doi.org/10.3847/1538-4357/ab44a9

Testing the Radius Scaling Relation with *Gaia* DR2 in the *Kepler* Field

Joel C. Zinn[1,2,3], Marc H. Pinsonneault[2], Daniel Huber[4], Dennis Stello[1,5,6,7], Keivan Stassun[8,9], and Aldo Serenelli[10,11]
[1] School of Physics, University of New South Wales, Barker Street, Sydney, NSW 2052, Australia; j.zinn@unsw.edu.au
[2] Department of Astronomy, The Ohio State University, 140 West 18th Avenue, Columbus, OH 43210, USA
[3] Kavli Institute for Theoretical Physics, University of California, Santa Barbara, CA 93106, USA
[4] Institute for Astronomy, University of Hawai'i, 2680 Woodlawn Drive, Honolulu, HI 96822, USA
[5] Sydney Institute for Astronomy (SIfA), School of Physics, University of Sydney, NSW 2006, Australia
[6] Stellar Astrophysics Centre, Department of Physics and Astronomy, Aarhus University, Ny Munkegade 120, DK-8000 Aarhus C, Denmark
[7] Center of Excellence for Astrophysics in Three Dimensions (ASTRO-3D), Australia
[8] Vanderbilt University, Department of Physics & Astronomy, 6301 Stevenson Center Ln., Nashville, TN 37235, USA
[9] Fisk University, Department of Physics, 1000 17th Ave. N., Nashville, TN 37208, USA
[10] Institute of Space Sciences (ICE, CSIC) Campus UAB, Carrer de Can Magrans, s/n, E-08193, Bellaterra, Spain
[11] Institut d'Estudis Espacials de Catalunya (IEEC), C/Gran Capita, 2-4, E-08034, Barcelona, Spain
Received 2019 June 15; revised 2019 September 9; accepted 2019 September 12; published 2019 November 12

Abstract

We compare radii based on *Gaia* parallaxes to radii based on asteroseismic scaling relations for ∼300 dwarfs and subgiants and ∼3600 first-ascent giants from the *Kepler* mission. Systematics due to temperature, bolometric correction, extinction, asteroseismic radius, and the spatially correlated *Gaia* parallax zero-point contribute to a 2% systematic uncertainty on the agreement in *Gaia*–asteroseismic radius. We find that dwarf and giant scaling radii are on a parallactic scale at the level of $-2.1\% \pm 0.5\%$ (rand.) $\pm$ 2.0% (syst.) (dwarfs) and $+1.7\% \pm 0.3\%$ (rand.) $\pm$ 2.0% (syst.) (giants), supporting the accuracy and precision of scaling relations. In total, the 2% agreement that we find holds for stars spanning radii between 0.8 $R_\odot$ and 30 $R_\odot$. We do, however, see evidence for *relative* errors in scaling radii between dwarfs and giants at the level of $4\% \pm 0.6\%$, and find evidence of departures from simple scaling relations for radii above 30 $R_\odot$. Asteroseismic masses for very metal-poor stars are still overestimated relative to astrophysical priors, but at a reduced level. We see no trend with metallicity in radius agreement for stars with $-0.5 < [\mathrm{Fe/H}] < +0.5$. We quantify the spatially correlated parallax errors in the *Kepler* field, which globally agree with the *Gaia* team's published covariance model. We provide *Gaia* radii, corrected for extinction and the *Gaia* parallax zero-point, for our full sample of ∼3900 stars, including dwarfs, subgiants, and first-ascent giants.

Key words: asteroseismology – catalogs – parallaxes – stars: fundamental parameters – stars: low-mass

Supporting material: machine-readable table

1. Introduction

Stellar astrophysics is in the midst of a radical transformation. Massive surveys using a variety of tools—time domain, astrometric, photometric, and spectroscopic—are yielding a wealth of information about stars. This treasure trove is not merely far larger than prior data sets; it also contains fundamentally new information. This is particularly true for fields studied by the *Kepler* (Borucki et al. 2008) satellite, where we have detected stellar oscillations in hundreds of stars near the main sequence turnoff (e.g., Chaplin et al. 2011) and tens of thousands of evolved giant stars (e.g., Yu et al. 2018). The focus of this paper is to test the accuracy and precision of radii that have been derived from *Kepler* asteroseismology.

Virtually all cool stars excite solar-like oscillations. Most stellar population studies distill the information in the oscillation spectrum down to two characteristic fRequencies: the frequency of maximum power, $\nu_{\max}$, and the large frequency spacing, $\Delta\nu$. These can be related to stellar mass and radius through scaling relations. The frequency of maximum power is related to the acoustic cutoff frequency, and by extension the surface gravity and effective temperature (Brown et al. 1991; Kjeldsen & Bedding 1995). The large frequency spacing is related to the mean density, which can be demonstrated with asymptotic pulsation theory (Tassoul 1980; Christensen-Dalsgaard 1993). In simple scaling relations one therefore solves for two equations in two unknowns, yielding asteroseismic masses and radii as a function of $T_{\rm eff}$ and the asteroseismic parameters. With the addition of abundances from high-resolution spectra, stellar ages can also be derived. The APOGEE–*Kepler*, or APOKASC, collaboration was set up to take advantage of this exciting prospect.

APOGEE uses an infrared spectrograph with $R = 22{,}500$ in combination with the 2.5 m telescope of the Sloan Digital Sky Survey (SDSS) (Gunn et al. 2006). The temperature scale of APOGEE (Majewski et al. 2010) has been calibrated to agree with that of the infrared flux method (IRFM) (Holtzman et al. 2015), and the temperatures have recently been recalibrated to correct for evolutionary state– and metallicity-dependent trends in the most recent data release, DR14 (Holtzman et al. 2018).

Pinsonneault et al. (2014) combined APOGEE spectroscopic temperatures and metallicities with asteroseismic information for nearly 2000 giants in a forward-modeling exercise that reported typical precisions in mass and radius of 12% and 5%. This work represented the largest application of asteroseismology to determine fundamental stellar quantities, and clearly demonstrated the use of asteroseismology in work on stellar populations: the mass, radius, and surface gravity of thousands of stars could be shown to be reasonable and nominally extremely precise. Nevertheless, there was room for improvements. For instance, it seemed evident that there were evolutionary state-dependent systematics that could not be precisely characterized because the sample did not have asteroseismic classifications of evolutionary state. More fundamentally, the stellar parameters were not tested against a fundamental scale (interferometric radii, for example). Theoretically motivated corrections to $\Delta\nu$ were not applied to the

catalog, meaning that there were systematic offsets at the ≈10% level in the mass and radius scales for the red giant branch (RGB). Indeed, Epstein et al. (2014) would discover that APOKASC-I asteroseismic radii and masses were systematically offset compared to the old stellar population in the halo.

The APOKASC-2 catalog (Pinsonneault et al. 2018) improved upon its predecessor in these and other ways. The new catalog was calibrated to the dynamical mass scale from two clusters, NGC 6791 and NGC 6819. The catalog also contained evolutionary state information, theoretical $\Delta\nu$ corrections were applied, and a self-consistent asteroseismic scale and error budget were derived using asteroseismic parameters from five independent pipelines.

The current work capitalizes on this catalog to perform a test of the scaling relations themselves. With the stellar parameters calibrated to a fundamental scale, we can compare the calibrated radii from the catalog to radii from *Gaia*, effectively using each *Gaia* radius as its own fundamental calibrator. This allows us, ultimately, to have not two calibrators (the masses of the giant branches of NGC 6791 and NGC 6819), but thousands—testing the scaling relations at every radius, temperature, and metallicity in the sample; the fact that *Gaia* provides a distance to each star means that every star, in effect, is like an open cluster member. Knowing the distance, in combination with flux, means that one knows the luminosity, and thus, in combination with a temperature and the Stefan–Boltzmann law, the radius. This exercise therefore requires accurate and precise luminosities and temperatures that are not subject to systematic biases. In what follows, we take care to ensure that our luminosities and temperatures are well characterized.

In previous work, Huber et al. (2017) applied this technique using *Gaia* Data Release (DR) 1, and demonstrated that the Tycho–*Gaia* astrometric solution (TGAS) (Michalik et al. 2015; Gaia Collaboration et al. 2016) and asteroseismic radii agreed to within 5% for stars with radii of ≈0.8–8 $R_\odot$. A similar exercise was also performed with *Hipparcos* (van Leeuwen 2007) parallaxes (Silva Aguirre et al. 2012), indicating agreement at the 5% level. Sahlholdt & Silva Aguirre (2018) used *Gaia* DR2 parallaxes to test the dwarf asteroseismic radius scale, finding that it is concordant with *Gaia* radii at the 2%–3% level. The red clump radius scale has also been shown to agree with the *Gaia* radius scale at the 2% level (Hall et al. 2019). Most recently, a determination of the *Gaia* parallax zero-point by Khan et al. (2019) suggests good agreement between asteroseismic parallaxes and Gaia DR2 parallaxes among both first-ascent red giant branch and red clump stars.

The scaling relation radius scale has been tested in other work against other fundamental scales, which have all indicated that the asteroseismic radius scale is good to at least the 10% level. Asteroseismic radii have been tested against interferometric values (Huber et al. 2012a), for instance, demonstrating good agreement. There are a handful of studies comparing the asteroseismic scale to a dynamical scale using eclipsing binaries. Following studies of individual binary systems hosting a giant star by Frandsen et al. (2013) and Rawls et al. (2016), Gaulme et al. (2016) contributed the largest such analysis. All of the red giants from Gaulme et al. (2016) have dynamical and asteroseismic radii less than 15 $R_\odot$, and exhibit an offset at the 5% level in the sense that the asteroseismic radii are larger than the dynamical radii. Brogaard et al. (2018), however, using a subset of the sample of Gaulme et al. (2016), argued that a reanalysis of the stellar parameters brought the asteroseismic radii into agreement with the dynamical radii.

This paper models itself after Huber et al. (2017), improving upon those constraints thanks to the increased precision of *Gaia* DR2 (Gaia Collaboration et al. 2016, 2018) parallaxes over those from DR1. We also expand the analysis to include stars with a radius of up to ∼50 $R_\odot$. Here, we look at 4128 stars with asteroseismic radii and parallaxes from *Gaia* DR2, comprising 372 dwarfs and 3755 giants. Note that we are analyzing first-ascent RGB stars only; thus our giant sample is a subset of the nearly 7000 stars of APOKASC-2. Given that there are known red clump versus RGB systematics, we analyze red clump stars separately (M. H. Pinsonneault et al. 2019, in preparation).

A comparison of the *Gaia* DR2 radius scale and the asteroseismic radius scale will be sensitive to all of the scales involved: the luminosity scale (which depends on the *Gaia* parallax scale and the bolometric correction scale), the temperature scale, and the asteroseismic radius scale. In this work, we use *Gaia* parallaxes corrected according to Zinn et al. (2019) as a benchmark against which to compare the asteroseismic radius scale. We also quantify the systematic errors in the bolometric correction scale and the temperature scale by comparing to other scales established in the literature. We also quantify the spatial correlations in *Gaia* DR2 parallaxes for the *Kepler* field, following the example of Zinn et al. (2017). Such correlations are directly relevant to other population-level studies, which compute some sky-averaged statistic that combines quantities that depend on parallax (e.g., calculations of open cluster distance).

2. Data

Zinn et al. (2019) presented the basic *Gaia*–asteroseismic data set we use in this paper, and we review its properties here.

2.1. The Asteroseismic Comparison Samples

As mentioned in Section 1, asteroseismology offers so-called scaling relations, which are means of deriving stellar masses and radii based on the characteristic frequencies of solar-like oscillations, $\Delta\nu$ and $\nu_{\rm max}$. The radius scaling relation is the subject of study in this work, and takes the form

$$\frac{R}{R_\odot} \approx \left(\frac{\nu_{\rm max}}{f_{\nu_{\rm max}}\,\nu_{\rm max,\odot}}\right)\left(\frac{\Delta\nu}{f_{\Delta\nu}\,\Delta\nu_\odot}\right)^{-2}\left(\frac{T_{\rm eff}}{T_{\rm eff,\odot}}\right)^{1/2}. \quad (1)$$

This relation bears the qualification "scaling" because it rescales the solar values of $R_\odot$, $\nu_{\rm max,\odot}$, $\Delta\nu_\odot$, and $T_{\rm eff,\odot}$ based on relations between (1) $\Delta\nu$ and the density of a star (Tassoul 1980; Christensen-Dalsgaard 1993), and (2) $\nu_{\rm max}$ and the surface gravity and temperature of a star (Brown et al. 1991; Kjeldsen & Bedding 1995), formalized in their own scaling relations as follows:

$$\frac{\Delta\nu}{f_{\Delta\nu}\,\Delta\nu_\odot} \approx \sqrt{\frac{M/M_\odot}{(R/R_\odot)^3}} \quad (2)$$

and

$$\frac{\nu_{\rm max}}{f_{\nu_{\rm max}}\,\nu_{\rm max,\odot}} \approx \frac{M/M_\odot}{(R/R_\odot)^2\sqrt{T_{\rm eff}/T_{\rm eff,\odot}}}. \quad (3)$$

We use the same solar values for these quantities as used in constructing the APOKASC-2 catalog (Pinsonneault et al. 2018): $\nu_{\rm max,\odot} = 3076\ \mu$Hz, $\Delta\nu_\odot = 135.146\ \mu$Hz, and $T_{\rm eff,\odot} = 5772$ K.

Theoretically motivated corrections to observed $\Delta\nu$, denoted in the above equations as $f_{\Delta\nu}$, are required to bring the observed $\Delta\nu$ into agreement with the theoretical $\Delta\nu$ assumed in asymptotic pulsation theory. These corrections depend on the evolutionary state of the star, as well as the mass, temperature, surface gravity, and metallicity (e.g., Sharma et al. 2016). Similar corrections may be required of $\nu_{\rm max}$ (denoted $f_{\nu_{\rm max}}$ in the above equations), and, if present and not accounted for, would be a potential source of problems in the asteroseismic radius scale. Throughout the work, we assume $f_{\nu_{\rm max}} = 1$. We discuss the possibility that $f_{\nu_{\rm max}}$ departs from unity in a way that depends on metallicity in Section 4.3.1.

Using the asteroseismic radius scaling relation (Equation (1)), we derive radii, which we compare to *Gaia* radii. For the purposes of this work, we correct the asteroseismic radii using $f_{\Delta\nu}$ given their solid theoretical and empirical basis (e.g., White et al. 2011; Guggenberger et al. 2016; Sharma et al. 2016), and attempt to interpret remaining discrepancies in the asteroseismic radius scale in terms of proposed $\nu_{\rm max}$ corrections, $f_{\nu_{\rm max}}$. We test the radius scaling relation in four radius regimes: for the three largest radius regimes, we use a sample consisting of first-ascent RGB stars, and for the smallest radius regime, we use a sample consisting of dwarfs and subgiants. We describe these samples next.

2.1.1. Giants

The primary asteroseismic comparison sample in our study is one of ≈3800 RGB stars from the APOKASC-2 catalog (Pinsonneault et al. 2018), which have $\nu_{\rm max}$ and $\Delta\nu$ values that are averaged across five independent asteroseismology pipelines. Asteroseismic classifications of evolutionary state are derived from asteroseismology for all but ≈200 of these stars, with the remainder categorized as RGB stars based on spectroscopy (see Holtzman et al. 2018 for a description of the spectroscopic method). The value for $\nu_{\rm max,\odot}$ from Pinsonneault et al. (2018), which we also use in this work, was chosen to bring the mean asteroseismic mass into agreement with the dynamical masses of NGC 6791 and NGC 6819. A systematic error on the APOKASC-2 radii of 0.7% is thus inherited from the uncertainty on the open cluster dynamical masses. Temperatures for the radius scaling relation are taken from APOGEE DR14 (Holtzman et al. 2018), as are metallicities for the purposes of computing theoretical $f_{\Delta\nu}$ values. We have adopted theoretical $f_{\Delta\nu}$ from Pinsonneault et al. (2018), which are computed using a revised version of the Bellaterra Stellar Parameters Pipeline (BeSPP, Serenelli et al. 2013, 2017). Where noted, we have validated our results using an alternative $f_{\Delta\nu}$ prescription from Sharma et al. (2016). Our giants have asteroseismic radii greater than 3.5 $R_\odot$.

2.1.2. Dwarfs and Subgiants

The other asteroseismic comparison sample consists of ≈400 dwarfs and subgiants with asteroseismic parameters taken from Huber et al. (2017), which includes stars from a reanalysis of the sample of Chaplin et al. (2014) by Serenelli et al. (2017), as well as stars from Huber et al. (2013). As for the giants, effective temperatures and metallicities are taken from APOGEE DR14, and BeSPP $f_{\Delta\nu}$ are used. We only consider stars with radii less than 3.5 $R_\odot$ from this sample.[12]

The giant $\nu_{\rm max}$ and $\Delta\nu$ values in the APOKASC-2 catalog are on the mean asteroseismic scale, whereas those for our dwarfs and subgiants are natively on the SYD pipeline scale (Huber et al. 2009). We correct the asteroseismic parameters to bring them into alignment with the APOKASC-2 mean scale, which amounts to a negligible rescaling of $\nu_{\rm max}$ and $\Delta\nu$ by 0.06% and 0.05%. Considering we use BeSPP theoretical $f_{\Delta\nu}$ for both the giant and the dwarf/subgiant samples, the end result is that the $\nu_{\rm max}$ and $\Delta\nu$ values in our full sample spanning dwarfs and giants are on a consistent system.

2.2. The Gaia Data Release 2 Sample

Stellar parallax, ϖ_{Gaia}, constitutes the most important information from *Gaia*, which we use in combination with APOKASC-2 photometric information to derive radii against which we test the asteroseismic radius scale.

The *Gaia* DR2 parallaxes are of excellent quality, with typical statistical errors of 0.05 mas for the sort of bright stars that are in our sample. Some parallaxes, however, may be erroneous due to unresolved binary motions or statistical errors in the *Gaia* red and/or blue passband. We therefore apply quality cuts to the *Gaia* data according to Lindegren et al. (2018), by only selecting stars that fulfill the following criteria, which are the same as used in Zinn et al. (2019):

1. `astrometric_excess_noise` $= 0$;
2. $\chi \equiv \sqrt{\chi^2/n}$, $\chi < 1.2\max(1, \exp -0.2(G - 19.5))$;
3. `visibility_periods_used` > 8;
4. $1.0 + 0.015(G_{\rm BP} - G_{\rm RP})^2 <$ `phot_bp_rp_excess_factor` $< 1.3 + 0.06(G_{\rm BP} - G_{\rm RP})^2$;

where $\chi^2 \equiv$ `astrometric_chi2_al`, $n \equiv$ `astrometric_n_good_obs_al` - 5, $G_{\rm BP} =$ `phot_bp_mean_mag`, $G_{\rm RP} =$ `phot_rp_mean_mag`, $G =$ `phot_g_mean_mag`.

The first and second cuts remove stars with a bad parallax solution, which may be caused by unresolved binary motion. The third cut rejects stars whose *Gaia* observations are over time baselines that are not well separated, and therefore whose underlying astrometric data do not constrain the astrometric model very well. The fourth cut removes stars that are plagued by bad *Gaia* photometry. 43 stars were rejected by these cuts for the dwarf/subgiant sample, and 182 from the giant sample.

We apply a final quality cut to remove stars whose asteroseismic parallaxes (which are derived according to the next section) and *Gaia* parallaxes do not agree at the 5σ level. This cut is performed for each analysis method described in Section 3. One star from the dwarf/subgiant sample is rejected in this way, and 15 from the giant sample.

Photometric information and temperatures are required to compute a radius from a parallax and vice versa, as discussed in the next section. We adopt Two Micron All Sky Survey (2MASS; Skrutskie et al. 2006) $K_{\rm s}$ photometry, rejecting 11 RGB stars without reliable photometric uncertainty (photometric quality flag of "F"). We use APOGEE DR14 temperatures to perform these transformations. For the giants in our analysis, extinctions from Rodrigues et al. (2014) from the APOKASC-2 catalog are used to apply small de-extinction corrections to the infrared photometry. For the $K_{\rm s}$ extinction coefficient, we use the reddening law of Fitzpatrick (1999) applied to the 2MASS $K_{\rm s}$ passband, as implemented in `mwdust` (Bovy et al. 2016), assuming an $E(B - V)$ from Schlegel et al. (1998), as recalibrated by Schlafly & Finkbeiner (2011). The dwarf and subgiant extinction values are from Green et al. (2015).

Our final sample consists of 328 dwarfs/subgiants and 3554 RGB stars.

[12] One star present in both the sample of Serenelli et al. (2017) and our giant sample, KIC 10394814, was excluded from the dwarf/subgiant sample.

3. Methods

The naive approach to testing the asteroseismic radius scaling relation would be to compare APOKASC-2 asteroseismic radii to the radii released as part of *Gaia* DR2. However, the out-of-the-box *Gaia* DR2 radii were derived without modeling extinctions, without correcting for the known DR2 parallax zero-point errors, and with temperatures that are not on the same scale as the APOGEE DR14 temperatures used to compute our asteroseismic radii. Therefore, we compute our own set of radii using the *Gaia* DR2 parallaxes, and adopt temperatures and extinctions from APOKASC-2. To do this, we use the Stefan–Boltzmann law to invert a luminosity (from an observed flux and bolometric correction in combination with a *Gaia* DR2 distance) plus a temperature to yield a radius.

The *Gaia*–asteroseismology radius comparison requires not only a temperature, extinction, bolometric correction, and a scaling relation radius, but also a *Gaia* parallax, of course. The *Gaia* parallaxes suffer from a small but non-negligible zero-point offset that is position-dependent and appears to be dependent on color and magnitude as well. This needs to be taken into account. Fortunately, our data set spans a range in both radius and parallax/distance. That means that, for a given radius, there are stars that are very close by and stars that are far away. One the one hand, the nearby stars have relatively high parallax, and therefore their *Gaia* radii are not sensitive to a relatively small zero-point correction. On the other hand, the distant stars have a relatively low parallax, and their radii are sensitive to zero-point corrections. We use the range in distance in our sample to our advantage by applying our primary analysis to a subsample of our asteroseismic comparison sample consisting of stars with high parallaxes whose *Gaia* radii are therefore not sensitive to *Gaia* parallax zero-point errors. As we describe in the next section, we fit for radius correction factors among this subsample that bring the asteroseismic radius scale into agreement with the *Gaia* radius scale, after correcting the *Gaia* parallaxes according to Zinn et al. (2019). In practice, we do this by working in parallax space and not radius space: we use the Stefan–Boltzmann law to transform our asteroseismic radii, in combination with fluxes and temperatures, into distances/parallaxes. As we note in Section 3.6, the asteroseismic parallax is more sensitive to problems in the asteroseismic radius scale for high-parallax stars than low-parallax stars, which is another benefit of applying our primary analysis to high-parallax stars. The rest of the stars with lower parallaxes are then used to further validate the differential trends we see in the radius agreement as a function of evolutionary state (Section 4.2), and to validate the choice in our *Gaia* parallax zero-point correction (Section 5.2).

Elements of this approach are described in Zinn et al. (2019), wherein the authors derived a *Gaia* DR2 parallax zero-point for the *Kepler* field assuming that the asteroseismic radii were not subject to errors. This assumption is valid given the relative insensitivity of the inferred parallax offset to the asteroseismic radius scale (see their Figure 5(b)). We discuss this assumption further in Section 5.2, and demonstrate that the *Gaia* DR2 parallax zero-point we adopt does not bias our results. Ultimately, we use the *Gaia* DR2 parallax zero-point of Zinn et al. (2019) to correct the *Gaia* parallaxes and derive *Gaia* radii, against which we compare the asteroseismic radius scale.

To test the asteroseismic radius scale, we begin by constructing an asteroseismic parallax, $\varpi_{\rm seis}$, based on an effective temperature, $T_{\rm eff}$, and bolometric flux, F:

$$\begin{aligned}\varpi_{\rm seis}(T_{\rm eff}, F, R_{\rm seis}^{-1}) &= F^{1/2}\sigma_{\rm SB}^{-1/2}T_{\rm eff}^{-2}R_{\rm seis}^{-1} \\ &= f_0^{1/2}\,10^{-(1/5)(m+{\rm BC}-A_m)}\sigma_{\rm SB}^{-1/2}T_{\rm eff}^{-2}R_{\rm seis}^{-1},\end{aligned} \quad (4)$$

where the bolometric flux is computed based on a magnitude, m, a bolometric correction for that band, BC, a flux zero-point calibrated for that band, f_0, and an extinction in that band, A_m. $\sigma_{\rm SB}$ is the Stefan–Boltzmann constant, and the stellar radius, R, is taken to be the asteroseismic radius, $R_{\rm seis}$, which is derived from the radius scaling relation (Equation (1)).

Like the approach from Zinn et al. (2019), we then model the differences in asteroseismic and *Gaia* parallaxes. In that work, the authors fit a three-parameter model that described a global, color- and magnitude-dependent parallax zero-point such that the asteroseismic parallaxes and *Gaia* parallaxes agreed. In this work, we adopt the zero-point from Zinn et al. (2019), and then fit for asteroseismic radius correction factors that minimize the difference between the two parallax scales. We describe this model in the next section.

3.1. Scaling Radius Correction Model

We are interested in comparing asteroseismic radii to those derived using classical constraints from a combination of L and $T_{\rm eff}$. As there are physical effects that could be radius-dependent, we begin by defining distinct radius regimes where we will test our agreement. We can therefore test not only for problems in the radius scaling relation, but also whether the asteroseismic–*Gaia* radius agreement is different for evolved stars in different radius regimes. The smallest radius regime that we explore is the dwarf/subgiant regime, with radii less than $3.5\,R_\odot$, and down to $\approx 0.8\,R_\odot$. The other radius regimes we consider are all stages on the first-ascent RGB. The low-luminosity RGB stars below the radius of the red clump, $3.5\,R_\odot \leqslant R \leqslant 10\,R_\odot$, and more evolved RGB stars with $10\,R_\odot < R < 30\,R_\odot$ comprise the next two radius regimes. The largest radii that we consider in our analysis are those for which $R \geqslant 30\,R_\odot$.

In order to identify problems in the asteroseismic radius scale, we fit for an asteroseismic radius correction factor in each of the above radius regimes. We do so after correcting for the *Gaia* parallax zero-point described by a global offset, $c = 52.8\ \mu$as; an offset dependent on astrometric pseudo-color ($\nu_{\rm eff}$), $d = -151.0\ \mu$as μm; and a *Gaia* G-band magnitude-dependent offset, $e = -4.20\ \mu$as mag^{-1} (Zinn et al. 2019). We fit for the radius anomalies, a_1, a_2, a_3, and a_4, such that they minimize the difference between $\hat{\varpi}_{\rm seis}$ and $\hat{\varpi}_{Gaia}$. In parallax space, this is written as

$$\hat{\varpi}_{Gaia} = \begin{cases} a_1\hat{\varpi}_{\rm seis} - z & R < 3.5\,R_\odot \\ a_2\hat{\varpi}_{\rm seis} - z & 3.5\,R_\odot \leqslant R \leqslant 10\,R_\odot \\ a_3\hat{\varpi}_{\rm seis} - z & 10\,R_\odot < R < 30\,R_\odot \\ a_4\hat{\varpi}_{\rm seis} - z & R \geqslant 30\,R_\odot, \end{cases} \quad (5)$$

where z describes the *Gaia* parallax zero-point correction:

$$z = c + d(\hat{\nu}_{\rm eff} - 1.5) + e(\hat{G} - 12.2). \quad (6)$$

We turn our model for $\hat{\varpi}_{\rm seis} - \hat{\varpi}_{Gaia}$ into a likelihood by assuming Gaussian errors and a covariance matrix describing the covariance in parallax space of two stars, i and j, separated

by an angular distance, $\Delta\theta_{ij}$, which reads

$$C_{ij}(\Delta\theta_{ij}) = \chi(\Delta\theta_{ij})\sigma_{\varpi_{Gaia,i}}\sigma_{\varpi_{Gaia,j}} + \delta_{ij}\sigma_i^2, \quad (7)$$

where $\chi(\Delta\theta_{ij})$ is the spatial correlation in the parallaxes of the stars (see Appendix B), $\sigma_{\varpi_{Gaia,i}}$ is the *Gaia* parallax error for star i, σ_i is the uncertainty on $\hat{\varpi}_{\mathrm{seis},i} - \hat{\varpi}_{Gaia,i}$, and δ_{ij} is the Kronecker delta function. Hence, for $i = j$, $C_{ij}(\Delta\theta_{ij} = 0) = \sigma_i^2 = \sigma^2_{\varpi_{Gaia,i}} + \sigma^2_{\varpi_{\mathrm{seis},i}}$. We defer a discussion of the off-diagonal elements of C to Appendix B, and report our result for radius agreement (Section 4.1) with and without spatial parallax correlation terms in C. Our results are unaffected by the level of spatial correlation present in the high-parallax subsample due to the sparsity of these stars in the *Kepler* field. If we were making inferences using the full sample of ∼3900 stars, these spatial correlations would inflate uncertainties in averaged values at the 10% level.

We therefore write the likelihood for the parameters of interest, a_1, a_2, a_3, and a_4, as

$$\begin{aligned}&\mathcal{L}(a_1, a_2, a_3, a_4|c, d, e, \hat{\varpi}_{Gaia}, \hat{T}_{\mathrm{eff}}, \hat{\Delta\nu}, \hat{\nu}_{\mathrm{max}}, \hat{A}_V, \\ &\hat{K}_{\mathrm{s}}, \hat{\mathrm{BC}}, \hat{G}, \hat{\nu}_{\mathrm{eff}}) \\ &\propto \frac{1}{\sqrt{(2\pi)^N \det C}} \exp\left[-\frac{1}{2}(\boldsymbol{y} - \boldsymbol{x})^{\mathrm{T}} C^{-1} (\boldsymbol{y} - \boldsymbol{x})\right],\end{aligned} \quad (8)$$

where

$$\boldsymbol{y} \equiv \begin{cases} a_1\hat{\varpi}_{\mathrm{seis}}(\hat{T}_{\mathrm{eff}}, \hat{\Delta\nu}, \hat{\nu}_{max}, \hat{A}_V, \hat{K}_{\mathrm{s}}, \hat{\mathrm{BC}}) & R < 3.5\,R_\odot \\ a_2\hat{\varpi}_{\mathrm{seis}}(\hat{T}_{\mathrm{eff}}, \hat{\Delta\nu}, \hat{\nu}_{max}, \hat{A}_V, \hat{K}_{\mathrm{s}}, \hat{\mathrm{BC}}) & 3.5\,R_\odot \leqslant R \leqslant 10\,R_\odot \\ a_3\hat{\varpi}_{\mathrm{seis}}(\hat{T}_{\mathrm{eff}}, \hat{\Delta\nu}, \hat{\nu}_{max}, \hat{A}_V, \hat{K}_{\mathrm{s}}, \hat{\mathrm{BC}}) & 10\,R_\odot < R < 30\,R_\odot \\ a_4\hat{\varpi}_{\mathrm{seis}}(\hat{T}_{\mathrm{eff}}, \hat{\Delta\nu}, \hat{\nu}_{max}, \hat{A}_V, \hat{K}_{\mathrm{s}}, \hat{\mathrm{BC}}) & R \geqslant 30\,R_\odot \end{cases}$$

and

$$\boldsymbol{x} \equiv \hat{\varpi}_{Gaia} + c + d(\hat{\nu}_{\mathrm{eff}} - 1.5) + e(\hat{G} - 12.2).$$

The only free parameters in our asteroseismic radius correction model are a_1, a_2, a_3, and a_4 because c, d, e are fixed to the values from Zinn et al. (2019). We fit for the mean values and uncertainties in $\{a_1, a_2, a_3, a_4\}$ with the Markov chain Monte Carlo (MCMC) method, as implemented with the `emcee` package (Foreman-Mackey et al. 2013). To do so, we work with the posterior probability for $\{a_1, a_2, a_3, a_4\}$, which is the likelihood multiplied by any priors we may have on the parameters. We apply the priors that the radius correction factors should not be larger than 1.2 or less than 0.8, which is borne out by previous studies that find that problems in the radius scaling relations appear to be at less than the 5% level (Gaulme et al. 2016; Huber et al. 2017; Brogaard et al. 2018; Sahlholdt & Silva Aguirre 2018).

In this work, we adopt an infrared bolometric correction. This choice means that the bolometric correction is much less dependent on temperature because the K_{s} band is only linearly sensitive to temperature for a blackbody with the temperature of a cool giant (instead of exponentially sensitive in the visual band). Effects due to dust absorption are also markedly reduced in the infrared compared to the visual. The bolometric correction is interpolated from MIST bolometric correction tables (Paxton et al. 2011, 2013, 2015; Choi et al. 2016; Dotter 2016), which are computed from the C3K grid of 1D atmosphere models (C. Conroy et al. 2019, in preparation; based on ATLAS12/SYNTHE; Kurucz 1970, 1993). We discuss the effects of our choice of bolometric correction in Section 3.2.

3.2. Systematics Due to the Luminosity Scale

The luminosities that enter into our radius comparison have two components that admit systematic uncertainties: the bolometric flux scale and the parallax scale.

The parallax systematic is easily understood to be an additive systematic, since our radius comparison is performed by converting asteroseismic radii into parallaxes (Equation (5)). By adopting the *Gaia* parallax zero-point from Zinn et al. (2019), we admit a systematic uncertainty of 8.6 μas in our parallax difference comparison (Equation (5)) due to the uncertainty on c (Equation (6)). This corresponds to a ≈1.3% systematic in radius space for a typical giant in our sample, and even less among our dwarfs and subgiants because they have higher parallaxes.

Systematics in the bolometric correction and extinction scales enter into our analysis when converting an asteroseismic radius into an asteroseismic parallax via the flux term, F, in Equation (4). This means that a systematic in the bolometric correction or extinction of X mag introduces an $\frac{X}{2}$% systematic in our radius comparison. We explore the sensitivity of our reported radius correction factors for giants to the choice of bolometric correction and extinction by using an alternative extinction scale and five alternative bolometric corrections.

The extinction scale is tested using a spectral energy distribution (SED) approach, and it also provides an independent check on the bolometric correction. With the SED method, a bolometric correction is not required because the entire SED is fitted, and extinction is computed simultaneously, based on the SED shape. This process is described in Stassun & Torres (2016) and Stassun et al. (2017). We have also tested the robustness of our results by using the IRFM bolometric flux scale of González Hernández & Bonifacio (2009), the K_{s}-band bolometric flux scale from the same reference, the MIST g-band bolometric flux scale, and the V-band bolometric flux scale of Flower (1996). More details on these checks of bolometric correction and extinction systematics are found in Appendix A.

Between the self-consistency of the MIST bolometric corrections and comparisons to independent systems described further in Appendix A, we conclude that the K_{s}-band bolometric correction may have a systematic error of up to 1.9%, meaning that the radii are good to at least 1.0%, which we take as a systematic error due to the choice of bolometric correction and extinction.

3.3. Systematics Due to the Temperature Scale

Our radius comparison is more sensitive to temperature scale systematics than the above luminosity systematics because $R_{\mathrm{seis}}/R_{Gaia} \propto T^{5/2}$ as opposed to $R_{\mathrm{seis}}/R_{Gaia} \propto L^{-1/2}$ (see Equations (1) and (4)). The APOGEE DR14 temperatures we adopt for both giants and dwarf/subgiants have been calibrated to be on the IRFM scale of González Hernández & Bonifacio (2009). Therefore, the predominant systematic possible in the temperature scale used in this work is the systematic in the fundamental IRFM scale. Work on the IRFM scale dates back

decades (Blackwell & Shallis 1977; Blackwell et al. 1980), and has had widespread application in astronomy due to its relative insensitivity to metallicity, surface gravity, and model atmospheres (e.g., Arribas & Martinez Roger 1987; Alonso et al. 1994). Recently, Casagrande et al. (2010) determined that the IRFM scale for dwarfs and subgiants is good to at least 30–40 K when comparing to other temperature scales. They concluded that any small temperature systematics that may exist in the IRFM scale are likely due to the underlying accuracy of infrared photometric calibrations and Vega zero-points. Similarly, in the giant regime, González Hernández & Bonifacio (2009) found that their IRFM implementation agreed to within ≈40 K with the prevailing application of IRFM temperature to giants in the literature (Alonso et al. 1999), for the metallicity range of the majority of stars considered in this work ($-0.4 < [\mathrm{Fe/H}] < 0.4$). These systematics, when taken to be 2σ errors, imply that there is a systematic uncertainty in the radius scale due to the temperature scale used in this work of up to 1.1% at the 1σ level. Because the APOGEE temperatures are adjusted to be on a fundamental scale, any inferred temperature difference must therefore be in the fundamental system, not on uncalibrated spectroscopic measurements that have much larger systematics (see Casagrande et al. 2010 for an extensive discussion.)

3.4. Systematics Due to the Asteroseismic Radius Scale

Note that due to the calibration of the APOKASC-2 asteroseismic data to open cluster dynamical masses, the asteroseismic radii for giants and dwarfs/subgiants port over a systematic uncertainty of 0.7% from the random uncertainty of the dynamical mass scale. This means that when we go on to test the asteroseismic radius scale, all the reported agreements have an implicit systematic uncertainty of 0.7%.

3.5. Total Systematic Uncertainty in Radius Comparison

Adding in quadrature the systematic uncertainties from Sections 3.2–3.4, we estimate a total systematic uncertainty of 2.0% in our comparison of *Gaia* and asteroseismology radius scales.

3.6. A Subsample for Determining the Absolute Accuracy of the Scaling Relations

The primary goal of this work is to test the accuracy of the radius scaling relation. To do so, we need to ensure that the *Gaia* parallaxes themselves are on an absolute scale. Zinn et al. (2019) have looked at the issue of zero-point errors in *Gaia* parallaxes by assuming that the asteroseismic parallaxes were on an absolute scale and correcting the *Gaia* parallaxes to minimize the difference between the two scales. They showed that problems in asteroseismic radius of the sort we are looking for in this work would manifest as a difference in *Gaia* and asteroseismic parallax scales that is larger at higher parallaxes (see their Figure 2). Furthermore, any *Gaia* zero-point errors are not as important among high-parallax stars as they are for low-parallax stars (see Section 5.2). For these two reasons, we constructed a high-parallax subsample consisting of stars with $\varpi > 1$ mas, which will be the population from which we infer our best-fitting model for the asteroseismic radius correction model (Equation (5)). Its distributions in the H-R diagram and in parallax–radius space are shown in Figures 1(b) and 2(b). To compute the absolute magnitudes, we used distances based on

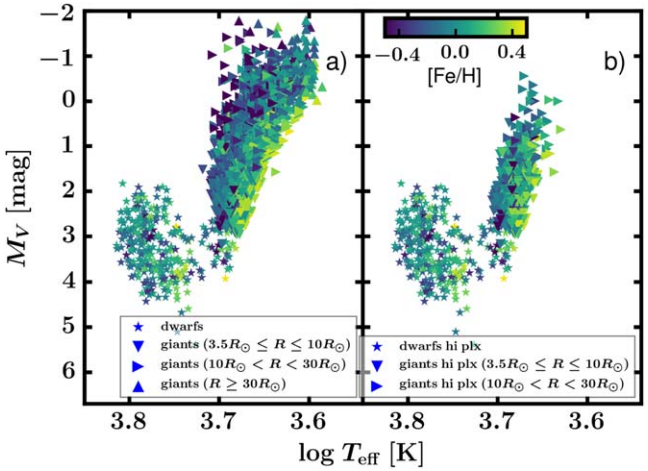

Figure 1. H-R diagram showing the full giant and dwarf/subgiant samples (left) and the high-parallax subsample (right) used in this work, divided into the four different radius regimes we consider.

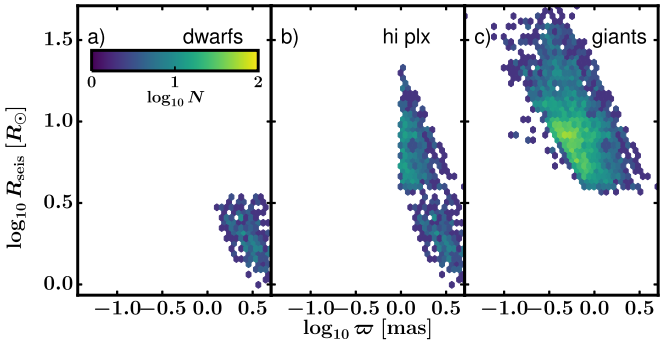

Figure 2. The distribution in parallax–radius space of the dwarf sample (left), the high-parallax subsample (middle), and the full giant sample (right) used in this work.

Gaia DR2 parallaxes, calculated following Bailer-Jones et al. (2018), by using the mode of the likelihood with an exponentially decreasing volume density prior with scale length 1.35 kpc. All of the dwarfs and subgiants are included in this subsample, given their relatively close distances. However, none of the stars with $R \geqslant 30\,R_\odot$ has a parallax that satisfies the high-parallax subsample selection criterion of $\varpi > 1$ mas. Therefore, a_4 is inferred using all of the stars with $R \geqslant 30\,R_\odot$, regardless of parallax. As we argue in Section 5.2, it does not appear that a_4 should be significantly biased by this choice.

3.7. A Sample for Determining Differential Corrections to the Radius Scaling Relation along the Giant Branch

Whereas we believe the high-parallax sample described in the previous section gives the best estimate of corrections to the asteroseismic radius scaling relation, we can also evaluate the agreement between *Gaia* and asteroseismic radius for stars at all parallaxes, and with a larger number of stars than the high-parallax subsample. For this purpose, we use all of our giant sample, whose distributions in the H-R diagram and in parallax–radius space are shown in Figures 1(a) and 2(c). This sample, which includes low-parallax stars, will also prove useful for demonstrating that *Gaia* parallaxes have been adequately corrected for the zero-point offsets (see Section 5.2).

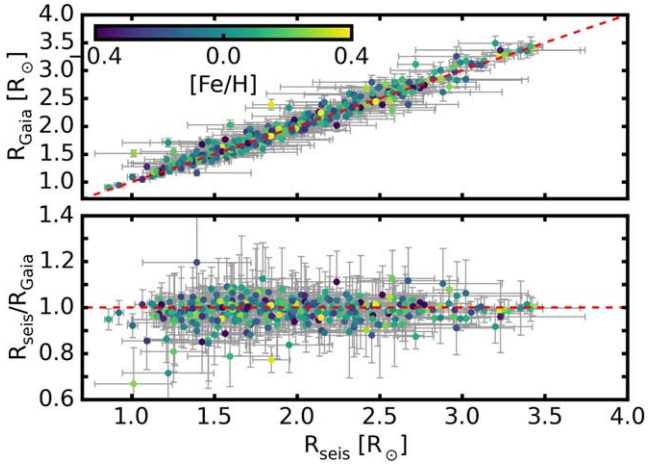

Figure 3. Comparison of radii derived using *Gaia* DR2 parallaxes with radii calculated from asteroseismic scaling relations for the sample in Huber et al. (2017). Color-coding denotes the metallicity for each star. The average residual median and scatter are ∼2% and ∼5%, respectively.

4. Results

4.1. Absolute Radius Agreement

Figure 3 compares asteroseismic and *Gaia* radii for dwarfs/subgiants, color-coded by metallicity, and plotted without any radius correction factor applied to the asteroseismic radii. The agreement is excellent, with a median offset of ≈2% and scatter of ≈5%. We observe no strong dependence of the residuals on metallicity, consistent with the results for the larger and more evolved giant sample discussed in Section 4.3.1. The radius correction factor we find in this, the smallest radius regime we consider ($R < 3.5\,R_\odot$), is $a_1 = 0.979 \pm 0.005$ (rand.) $\pm$ 0.020 (syst.). This means that the asteroseismic radius scale for dwarfs and subgiants agrees with the *Gaia* radius scale within the uncertainties.

Figure 4(a) shows our main result in the giant regime: asteroseismic radii agree with those from *Gaia* within 2.1% $\pm$ 2.0% (syst.). Figure 4(b) indicates the residuals when the parallaxes are only corrected by a zero-point offset (c in Equation (6)). Figure 4(c) shows the agreement after an additional correction with color- and magnitude-dependent terms (d and e in Equation (6)). Finally, Figure 4(d) shows the agreement after additionally applying the best-fitting radius correction factors from Equation (5). Irrespective of the *Gaia* zero-point model, and across a wide range in radius, the agreement between asteroseismic and *Gaia* radii is excellent.

Our best-fitting model that we assume in Figure 4(d) is fit using the high-parallax subsample of our giants ("K MIST" in Table 1) described in Section 3.6. The radius correction factors on the RGB of $\{a_2, a_3, a_4\} = (1.015 \pm 0.003$ (rand.) $\pm$ 0.020 (syst.), 1.019 ± 0.006 (rand.) $\pm$ 0.020 (syst.), 1.087 ± 0.009 (rand.) $\pm$ 0.020 (syst.)) indicate that the only statistically significant deviation in the asteroseismic radius scale from the *Gaia* radius scale is among the most evolved giants.

At radii larger than $30\,R_\odot$, non-adiabatic effects should begin to manifest in the atmosphere, certainly leading to breakdowns in the scaling relations (Mosser et al. 2013; Stello et al. 2014). $R > 30\,R_\odot$ also roughly corresponds to the same gravity regime ($\log g < 1.6$) in which Pinsonneault et al. (2018) found that the APOKASC-2 asteroseismic masses were offset from what the giant branch masses should be in the clusters NGC 6791 and NGC 6819. These evolved stars with $R \geqslant 30\,R_\odot$ may have a radius scale that is too large compared to the parallactic radius scale: their radius correction factor (a_4 in Equation (5)) corresponds to a radius inflation of 8.7% $\pm$ 0.9% (rand.) $\pm$2.0% (syst.). In this regime, the asteroseismic measurement of ν_{max} in this regime is ill-defined, given the small number of excited modes, and may therefore be systematically biased. Whether due to measurement systematics or due to the physical assumptions in the ν_{max} and $\Delta\nu$ scaling relations themselves no longer being valid (Equations (3) and (2)), the result is that the radius scaling relation as it is commonly used appears to break down for $R \geqslant 30\,R_\odot$.

In Table 1, we provide a_2 and a_3 for different choices of bolometric correction, extinction, and temperature. The agreement of a_2 and a_3 for these different test cases is generally within the systematic error due to bolometric correction and extinction of 1%. We discuss such systematic differences further in our solution in Section 5.2.

4.2. Differential Radius Agreement

As we mention in Section 3.7, thanks to the larger number of stars in the full giant sample compared to just the high-parallax giant subsample (see Figure 4(d) gray points versus navy points), the full giant sample gives an indication of differential trends in the asteroseismology–*Gaia* radius agreement.

First and foremost, there is a hint of a differential trend in the radius agreement in the regime $0.8\,R_\odot \lesssim R \lesssim 30\,R_\odot$, which can be seen in Figure 5(b). Although adjacent radius regimes yield radius correction factors that are statistically consistent with each other (e.g., the flat trend among just giants with $R < 30\,R_\odot$ seen in Figure 5(b)), when considering the radius correction factors required for dwarfs/subgiants ($a_1 = 0.979 \pm 0.005$) and for stars with $10\,R_\odot < R < 30\,R_\odot$ ($a_3 = 1.019 \pm 0.0060$), they are not statistically consistent with each other at the 5σ level. One explanation of this trend with radius would be a variation of the underlying physics determining the relationship between asteroseismic frequencies and stellar parameters as a function of radius. Such trends are supposed to be removed by $f_{\Delta\nu}$, but small inadequacies in $f_{\Delta\nu}$ could result in radius-dependent asteroseismic radius errors. This differential trend could also be caused by small systematic trends in the underlying measurements. For instance, small radius-dependent ν_{max} trends are noted by Pinsonneault et al. (2018); it is also feasible that there exists a small temperature offset between APOGEE dwarf and giant temperature scales. The second trend of note is that the asteroseismic radius scale appears to increasingly overpredict radii compared to *Gaia* for $R \gtrsim 30\,R_\odot$. The statistical significance of this trend is convincing in the sense that there is a bona fide radius inflation, but further work must be done to understand the asteroseismic radius scale for the upper giant branch—both observationally and theoretically—before commenting further on it. These trends are statistically significant, even when perturbing the temperature scale, as we note in Section 5.2.

4.3. Recommended Asteroseismic Radius Scale

According to our model for asteroseismic radius correction factors, dwarfs and subgiants have an asteroseismic radius scale that is too small at the 2% level, compared to the *Gaia* radius scale. As we noted in Section 4.1, the effect is not statistically significant, because it falls within the combined random and systematic uncertainty budget. The effect is reversed among

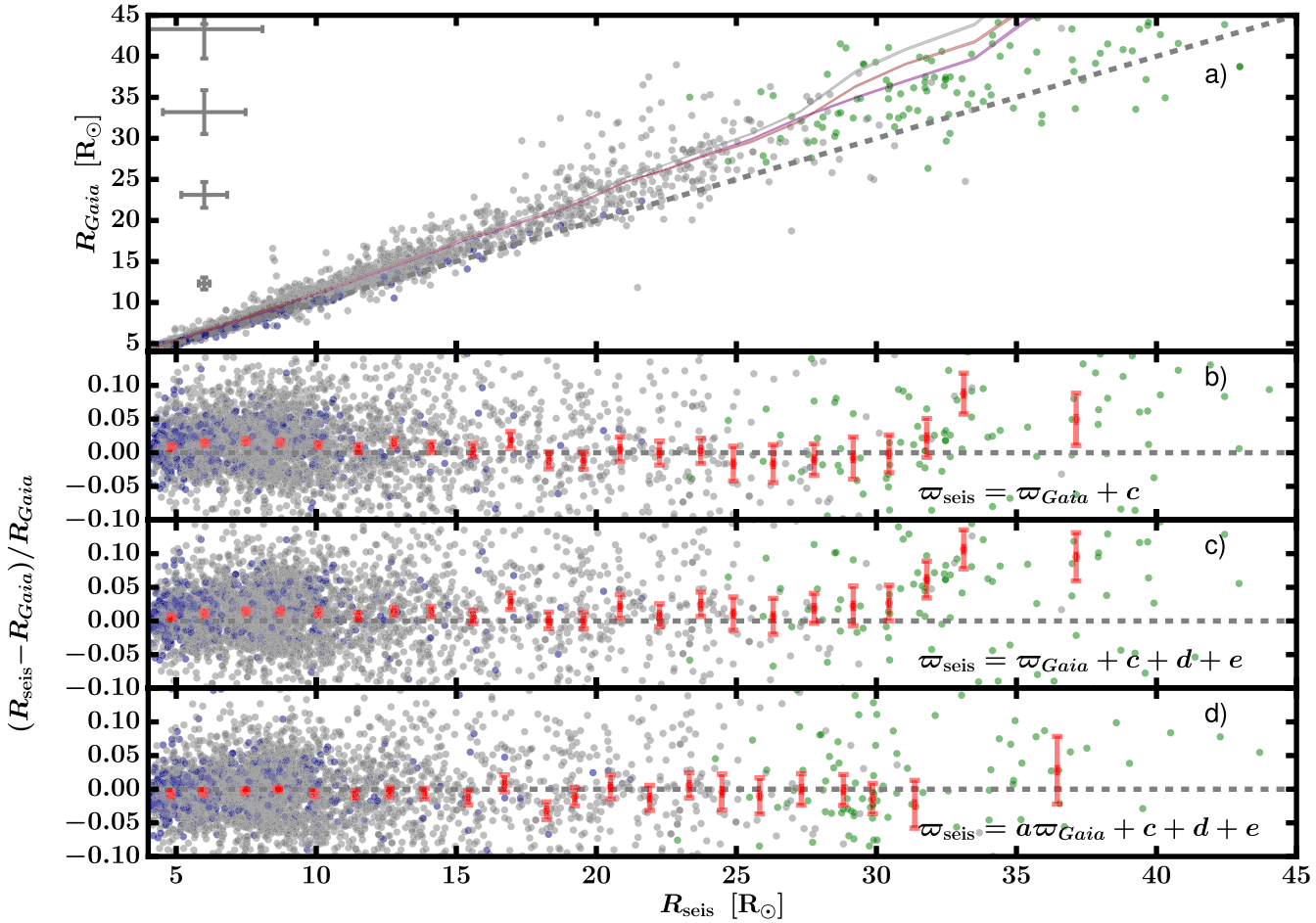

Figure 4. Asteroseismic RGB radii are in excellent agreement with *Gaia* radii, which indicates that the asteroseismic radius scaling relation is good to within 2% ± 2% up to radii of 30 $R_\odot$. Panel (a) shows *Gaia* radius as a function of asteroseismic radius for the giants in our sample. Green points are stars with surface gravities of $\log g < 1.6$ ($R \gtrsim 30\,R_\odot$) the regime in which there could be measurement-error related radius systematics (Pinsonneault et al. 2018). Navy points are stars that are part of the sample used to fit radius correction factors for the giants, a_2, a_3, and a_4, which have *Gaia* parallaxes greater than 1 mas ("hi plx" in Figures 1 and 2). The error bars indicate median errors as a function of *Gaia* radius. Panels (b)–(d) show the residuals in the radius agreement after successively correcting the data according to the model of Equation (5), with red error bars showing binned uncertainties on the median: panel (b) includes a global offset to the *Gaia* parallaxes of 52.8 μas (brown curve in panel (a)); panel (c) further includes color- and magnitude-dependent terms of −151.0 μas μm and −4.20 μas mag^{-1} (gray curve in panel (a)); panel (d) finally also corrects the asteroseismic radii by factors $a_2 = 1.015 \pm 0.0025$, $a_3 = 1.019 \pm 0.0060$, and $a_4 = 1.087 \pm 0.0092$ (purple curve in panel (a)).

Table 1
Parameters for Corrections to Fitted Asteroseismic Radius Scaling Relation

Method	a_1	a_2	a_3	a_4	A_V (mag)	A_{Ks} (mag)	χ^2/dof	N
K MIST	0.979 ± 0.005	...	...	...	0.079	0.009	0.261*****	328
K MIST	...	1.015 ± 0.003	1.019 ± 0.006	...	0.104	0.012	0.579*****	566
K MIST	...	...	...	1.087 ± 0.009	0.212	0.024	1.722****	112
K MIST no cov	...	1.015 ± 0.002	1.019 ± 0.006	...	0.104	0.012	0.579*****	566
V	...	1.001 ± 0.003	0.992 ± 0.007	...	0.103	0.012	0.525*****	560
V MIST	...	1.017 ± 0.003	1.017 ± 0.008	...	0.103	0.012	0.511*****	560
IRFM	...	1.014 ± 0.002	1.014 ± 0.006	...	0.103	0.012	0.601*****	556
SED	...	0.996 ± 0.002	0.998 ± 0.007	...	0.104	0.012	0.690*****	531

Note. The best-fitting parameters a_1, a_2, a_3, and a_4 for Equation (5). Different choices of bolometric correction, extinction, temperature, and spatial correlation are considered for fitting a_2 and a_3. Asterisks denote the level of discrepancy with the expected χ^2 given the degrees of freedom; each asterisk (up to and including five) denotes 1σ in the significance of the discrepancy. Also noted are the median extinctions in the V and K_s bands. Our preferred results are from the "K MIST" case, as discussed in the text. All the solutions take into account spatial correlations in *Gaia* DR2 parallaxes except the "K MIST no cov" case. See text for details.

giants, in the sense that both stars below and stars above the red clump radius ($R \sim 10\,R_\odot$) indicate an *inflation* of the asteroseismic radius scale above the *Gaia* radius scale at the 2% level. We can interpret these radius scale disagreements as consistent with errors in some combination of bolometric correction, extinction, temperature, the APOKASC-2 asteroseismic radius calibration, and the *Gaia* zero-point, which in total allow for systematic shifts in the radius agreement at the 2% level.

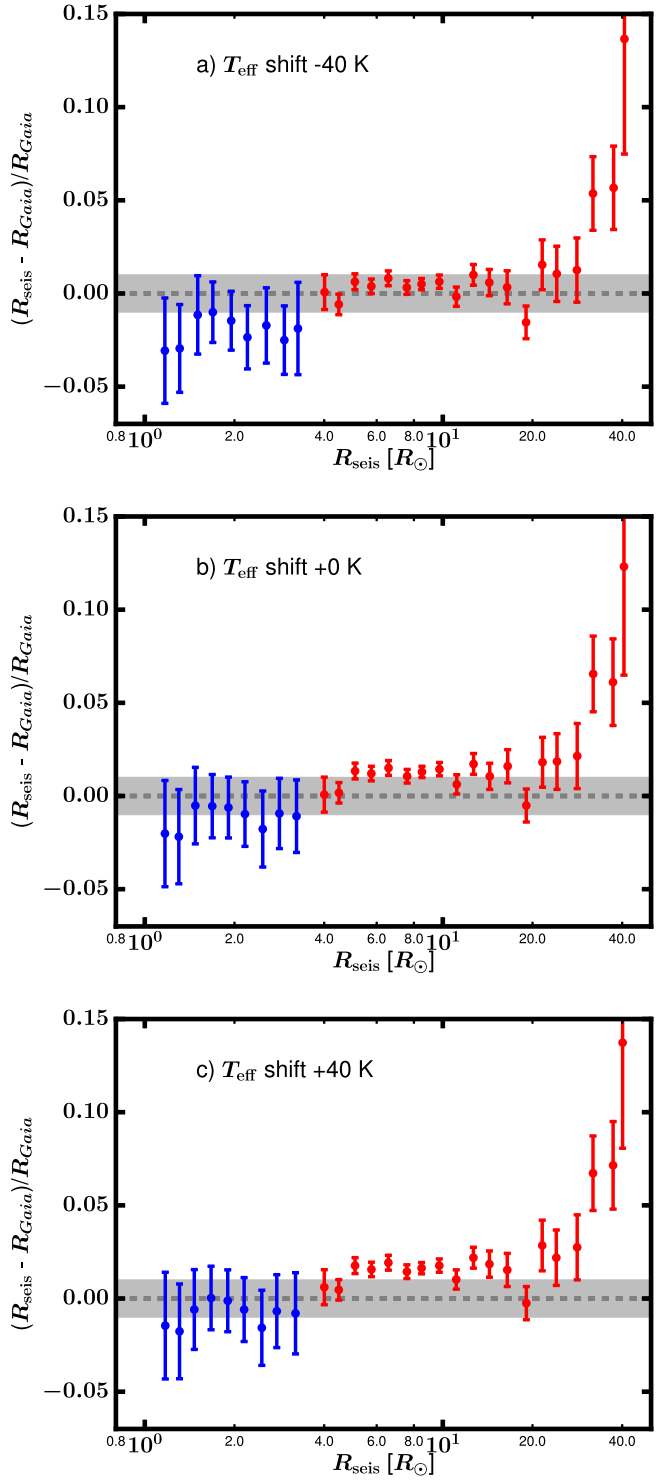

Figure 5. A close-up of Figure 4(c), but also including dwarfs/subgiants. The error bars are binned medians and the errors on the binned medians for the giant (red) and dwarf/subgiant (blue) samples. The gray band indicates the region of ±1% agreement. The agreement between asteroseismic and *Gaia* radii is good to within 2% ± 2% (syst.) for dwarfs, subgiants, and giants. Panel (a) shows the radius agreement if the APOGEE temperature scale is shifted downward by a 2σ systematic uncertainty on the temperature scale of 40 K, panel (b) shows the radius agreement with the APOGEE temperature scale unchanged, and panel (c) shows the radius agreement with the APOGEE temperature scale shifted upward by 40 K.

We therefore do not recommend specific corrections to the asteroseismic red giant radius scale, but rather conclude that the asteroseismic radius scale of giants, like that of dwarfs/subgiants, is consistent with the *Gaia* radius scale to within 2% ± 2% (syst.). The most evolved giants have asteroseismic radii that are inflated still further—by 9% ± 2% (syst.).

Table 2 contains the *Gaia* radii we have derived in this work. We provide both radii corrected for the *Gaia* parallax zero-point, and radii that have not been corrected. Note that a systematic uncertainty of 1.8% should be adopted for the corrected radii, which is smaller than our 2% systematic uncertainty on the ratio of *Gaia* and asteroseismic radii because of the smaller temperature dependence of the *Gaia* radii compared to the ratio of the two radius scales. The uncorrected *Gaia* radii are provided to use in conjunction with a custom *Gaia* zero-point, and their systematic uncertainty would be 1.6%, without taking into account systematics due to not correcting for the *Gaia* parallax zero-point. The radii corrected for parallax zero-point are plotted in Figure 6 as a function of temperature for both the full sample (panel (a)) and the high-parallax subsample (panel (b)).

4.3.1. Scaling Relations as a Function of Metallicity for [Fe/H] ⩾ −1

Based on the argument that scaling relations depend on the sound speed, and that the sound speed depends on molecular weight, Viani et al. (2017) have proposed that the $\nu_{\rm max}$ asteroseismic scaling relation (Equation (3)) should depend on metallicity. This theory would predict that $f_{\nu_{\rm max}}$ in Equations (1) and (3) would be non-unity and a function of metallicity. We can test this prediction with our data, by showing the parallax difference as a function of metallicity, as we do in Figure 7. Here, we have plotted the observed radius agreement as a function of [Fe/H], and have included the expected error in asteroseismic radius for the giants in the sample due to not including a molecular weight term in the scaling relations, according to Equation (21) of Viani et al. (2017) (brown band). The width of this band is due to the spread in [α/Fe], which we take from the APOKASC-2 catalog. We compute the molecular weight according to $\mu = 4/(3X + 1)$, assuming a helium enrichment of $\Delta Y/\Delta Z = 1$, a primordial helium abundance of $Y = 0.248$, $Z_\odot = 0.02$, and for each star in the sample, $Z = 10^{0.977[{\rm M/H}]-1.699}$ (Bertelli et al. 1994), where [M/H] = [Fe/H] + log(0.63810$^{[\alpha/{\rm Fe}]}$ + 0.362) (Salaris et al. 1993). The primary assumption in this simple implementation of a metallicity-dependent $f_{\nu_{\rm max}}$ is that there is a one-to-one relation between metallicity and helium fraction. A spread in intrinsic helium fraction would tend to smear out any trend with metallicity and therefore flatten the predicted effect. In our expression for mean molecular weight, we have also assumed that the gas is neutral within the acoustic radius of the star, which induces an uncertainty in the predicted metallicity-dependent radius error. There should also be an uncertainty due to not considering the adiabatic index in the atmosphere of the star, which will depend on metallicity. Investigating the impact of these effects would require detailed modeling of the stars, which is beyond the scope of this work. With these modeling caveats in mind, we see no evidence for the predicted metallicity effect across the more than 1 dex spread in metallicity shown in Figure 7. Indeed, the data are consistent with having no trend with metallicity to within 0.5% per dex for giants and 1.1% per dex for dwarfs/subgiants, based on least-squares fitting. Taking into account the 2% systematic uncertainty in our radius comparison does not change this conclusion, because the systematic is insensitive to metallicity, and therefore would tend to shift all of the data shown in

Table 2
A Subset of Our Recommended *Gaia* Radii, $R_{K_s,\mathrm{MIST}}$, and Their 1σ Random Uncertainties

KIC	$R_{K_s,\mathrm{MIST}}$ ($R_\odot$)	$\sigma_{R_{K_s,\mathrm{MIST}}}$ ($R_\odot$)	$R_{K_s,\mathrm{MIST,raw}}$ ($R_\odot$)	$\sigma_{R_{K_s,\mathrm{MIST,raw}}}$ ($R_\odot$)	Flags
11400880	9.75	0.71	11.08	0.88	20
6587865	21.63	1.50	25.64	2.03	30
5007332	6.79	0.44	7.40	0.50	20
5039087	21.98	2.39	31.30	4.61	30
4832196	16.61	1.24	19.78	1.71	30
10220213	4.38	0.23	4.54	0.24	21
10669876	13.12	0.62	14.14	0.69	30
4139784	10.04	0.43	10.72	0.47	30
3443483	6.33	0.28	6.65	0.30	20
6383574	23.42	1.38	27.17	1.75	30

Note. The full list is available online. We also include *Gaia* radii that have been computed without correcting the *Gaia* parallaxes, $R_{K_s,\mathrm{MIST,raw}}$. The listed uncertainties do not include systematic contributions to the uncertainties: there is a 1.8% systematic uncertainty on the zero-point-corrected *Gaia* radii and a 1.6% systematic uncertainty on the uncorrected *Gaia* radii, which does not account for the error induced by not correcting for the *Gaia* parallax zero-point. Flags are two digits in length: the first digit indicates to which of the four asteroseismic radius bins the star belongs (either 1, 2, 3, or 4 corresponding to Equation (5)), and the second digit is 1 if the star is a part of the high-parallax subsample, or 0 otherwise.

(This table is available in its entirety in machine-readable form.)

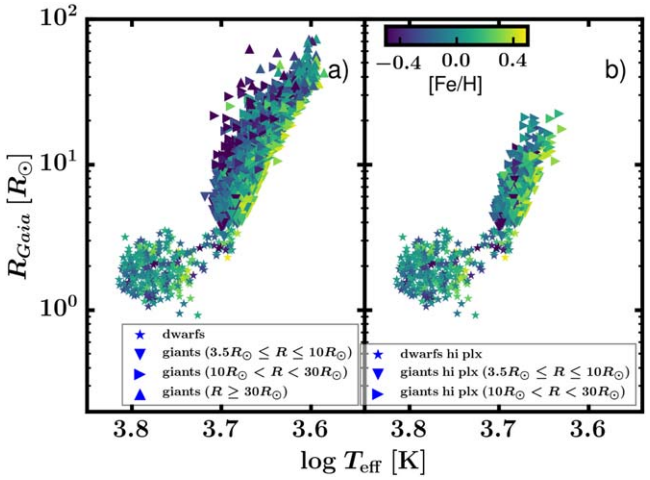

Figure 6. *Gaia* radii as a function of temperature for the full giant and dwarf/subgiant samples (left) and the high-parallax subsample (right) used in this work, divided into the four different regimes of asteroseismic radius we consider. These radii are excerpted in Table 2 in the column $R_{K_s,\mathrm{MIST}}$.

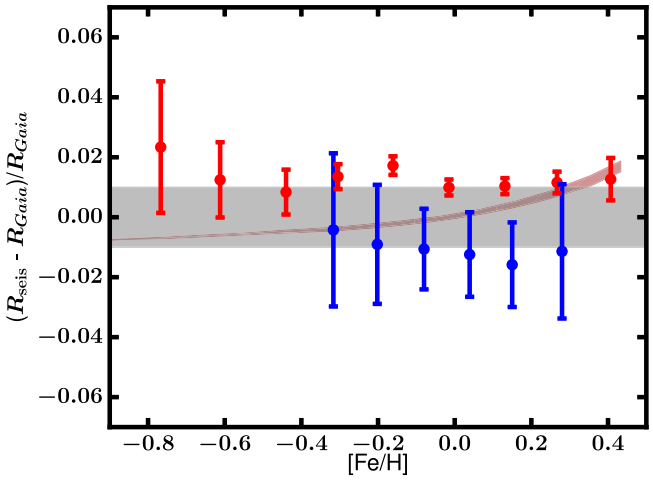

Figure 7. Difference between asteroseismic and *Gaia* parallax as a function of metallicity, after correction using our adopted *Gaia* parallax zero-point, but with no asteroseismic radius correction factors applied. The median and error on the median radius agreement in bins of metallicity are shown as red error bars for giants and as blue error bars for dwarfs/subgiants. The gray band indicates an agreement between the radius scales to within ±1%. The brown band indicates the expected disagreement from Viani et al. (2017) between the red giant radius scales with and without taking into account a molecular weight term. See Section 4.3.1 for details.

Figure 7 up or down. Until such a time as the intrinsic scatter in helium enrichment can be determined, which, at this point, hinders a comparison between the theoretical metallicity trend and the observed radius agreement, we conclude that the asteroseismic scaling relation radius does not require a metallicity term to within the precision afforded to us by our data set.

4.3.2. Scaling Relations for [Fe/H] < −1

Motivated by the observation in Epstein et al. (2014) that halo stars have asteroseismic masses that appear to be inflated compared to the masses expected from stellar models, we discuss here the asteroseismic radius and mass scale in the halo metallicity regime ([Fe/H] < −1). There seems to be no significant disagreement in radius space for the most metal-poor stars, which we show in Figure 8. Here, we have only shown the stars below the red clump ($R_{\rm seis} \leqslant 10\,R_\odot$) as black error bars, to disambiguate metallicity-dependent effects and radius scaling relation effects that we find in the most evolved stars (see Section 4.2). To isolate the metallicity effect, the a_2 radius correction factor is applied. When correcting for the radius correction factor derived from the high-parallax subsample at all metallicities as well as the parallax offset using the *Gaia* zero-point model from Zinn et al. (2019), which includes a color term, the radius anomaly of the eight stars with [Fe/H] < −1.0 and $R_{\rm seis} \leqslant 10\,R_\odot$ is 1.02 ± 0.02 (rand.) ± 0.02 (syst.) and thus does not deviate from unity. The color term (d in Equation (6)), however, will tend to correct for metallicity effects as well, if present. Even when only correcting the *Gaia* parallaxes using the radius correction factor and a global offset term, c, the anomaly is still not statistically significant, at 1.02 ± 0.02 (rand.) ± 0.02 (syst.). For this reason, there does not appear to be a problem with the asteroseismic radius scale at low metallicity.

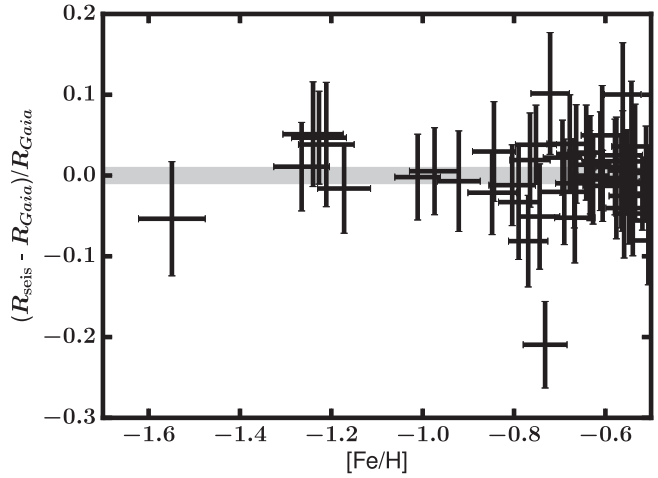

Figure 8. Fractional difference between asteroseismic and *Gaia* radius as a function of metallicity for low-metallicity stars with $R_{seis} \leqslant 10\,R_{\odot}$. A gray band corresponding to ±0.01 has been added to guide the eye. There is no statistically significant evidence for a metallicity-dependent asteroseismic radius error for [Fe/H] < −1.0. See Section 4.3.1 for details.

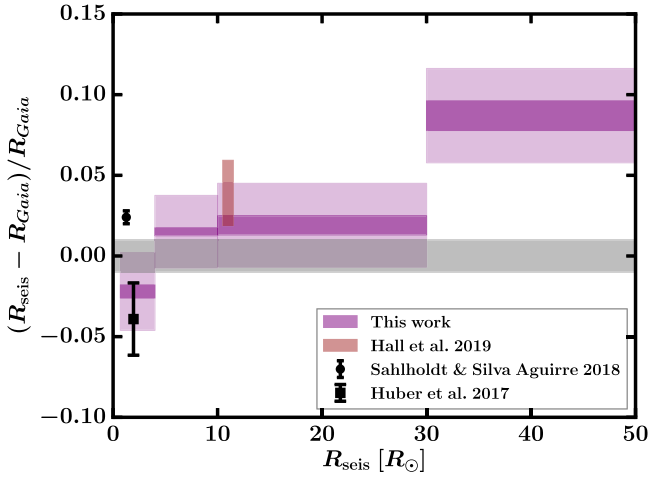

Figure 9. Comparison of asteroseismic–*Gaia* radius agreement among literature estimates and this work. The dark purple bands indicate the best-fitting radius correction factors that would bring asteroseismic radii into agreement with *Gaia* radii (Table 1), and the light purple bands indicate the 1σ systematic possible as a result of uncertainties in the luminosity scale, the temperature scale, and the asteroseismic radius scale. A gray band corresponding to ±0.01 has been added to guide the eye. See Section 5.1.1 for details.

We can also infer the corresponding inflation in mass space, by combining the mass scaling relation,

$$\frac{M_{\rm seis}}{M_{\odot}} \approx \left(\frac{\nu_{\rm max}}{f_{\nu_{\rm max}}\nu_{\rm max,\odot}}\right)^{3}\left(\frac{\Delta\nu}{f_{\Delta\nu}\Delta\nu_{\odot}}\right)^{-4}\left(\frac{T_{\rm eff}}{T_{\rm eff,\odot}}\right)^{3/2},$$

with a *Gaia* radius to yield a *Gaia* mass, which depends on both parallax and $\Delta\nu$:

$$\frac{M_{Gaia}}{M_{\odot}} \approx \left(\frac{\Delta\nu}{f_{\Delta\nu}\Delta\nu_{\odot}}\right)^{2}\left(\frac{R_{Gaia}}{R_{\odot}}\right)^{3}.$$

The assumption here is that $f_{\Delta\nu}$ corrects the scaling relation completely so that M_{Gaia} is unbiased, whereas the asteroseismic mass has an additional dependence on $\nu_{\rm max}$; looking at the ratio of *Gaia* to asteroseismic radius for a low-metallicity sample would reveal a metallicity-dependent $f_{\nu_{\rm max}}$. We have already inferred in Section 4 that there is a statistically insignificant but non-zero asteroseismic radius correction factor for stars with $R \leqslant 10\,R_{\odot}$ of $a_2 = 1.015$ averaged over the entire sample (with relatively high metallicities, mostly $-0.2 <$ [Fe/H] < 0.2). We find for these eight stars $\langle M_{Gaia}/M_{\rm seis}\rangle = 0.94 \pm 0.08$ (rand.) ± 0.07 (syst.) when correcting only for the radius correction factor and the *Gaia* global zero-point, and $\langle M_{Gaia}/M_{\rm seis}\rangle = 0.96 \pm 0.08$ (rand.) ± 0.07 (syst.) when also accounting for the color and magnitude terms. These ratios depart mildly from unity, but not strongly. Here, we have corrected the $\nu_{\rm max}$ scale for the effect of radius inflation we note in this paper, which lowers the asteroseismic mass scale by 4.5% given $R_{\rm seis} \propto \nu_{\rm max}$ and $M_{\rm seis} \propto \nu_{\rm max}^{3}$. The mass ratio we find is in agreement with that from Epstein et al. (2014), who found a mass ratio of 0.89 ± 0.04 when comparing halo and thick-disk masses expected from stellar models to asteroseismic masses corrected with $f_{\Delta\nu}$ according to the prescription of White et al. (2011). The strong temperature dependence, $M_{Gaia}/M_{\rm seis} \propto T^{-15/2}$, means that the ratio is particularly sensitive to temperature scale systematics, and so improvement upon these estimates of a metallicity effect may prove difficult even using a larger sample of halo stars.

5. Discussion

5.1. Comparison with Literature

5.1.1. Constraints from Gaia

We compare in Figure 9 the radius agreement we find in this work to recent work comparing the *Gaia* radius scale to the asteroseismic radius scale. First we consider the result from Hall et al. (2019), who performed a hierarchical Bayesian analysis of the red clump absolute magnitude in the $K_{\rm s}$ and *Gaia* G bands using both an asteroseismic luminosity and a *Gaia* luminosity. Using their best-fitting *Gaia* absolute luminosity in the $K_{\rm s}$ band of $\mu_{\rm RC,Gaia} = -1.634 \pm 0.018$ (which uses an uninformative prior on the *Gaia* parallax zero-point) and their best-fitting value using asteroseismology and APOKASC-2 temperatures of $\mu_{\rm RC,seis} = -1.693 \pm 0.003$ yields a radius agreement that is statistically consistent with the one inferred by us for RGB stars near the radius of the clump $R \sim 10\,R_{\odot}$. The constraint on absolute magnitude from Hall et al. (2019) is not a pure radius constraint, however, because the absolute magnitude depends on the luminosity and thus the temperature of the star. On the asteroseismic side, Hall et al. (2019) use temperatures either from APOKASC-2 or from Mathur et al. (2017). The former is the same temperature scale we adopt in this work, and so the agreement between red clump asteroseismic and *Gaia* absolute magnitudes from Hall et al. (2019) using the APOKASC-2 red clump stars would be an appropriate point of comparison to our constraints on the radius agreement along the first-ascent giant branch. However, the *Gaia* estimate of red clump absolute magnitude from Hall et al. (2019) is based on a sample of stars from the asteroseismic analysis of Yu et al. (2018), which have temperatures from Mathur et al. (2017) that are hotter on average than those from APOKASC-2. Taking into account this temperature effect results in a range of possible radius agreement on the red clump, which is shown in Figure 9 (the result of Hall et al. (2019) has been placed at a representative location on the abscissa in Figure 9 of $R = 11\,R_{\odot}$ and with a spread of $1\,R_{\odot}$, according to their Figure 2). We see agreement within the uncertainty between the radius of Hall et al. (2019) and the result

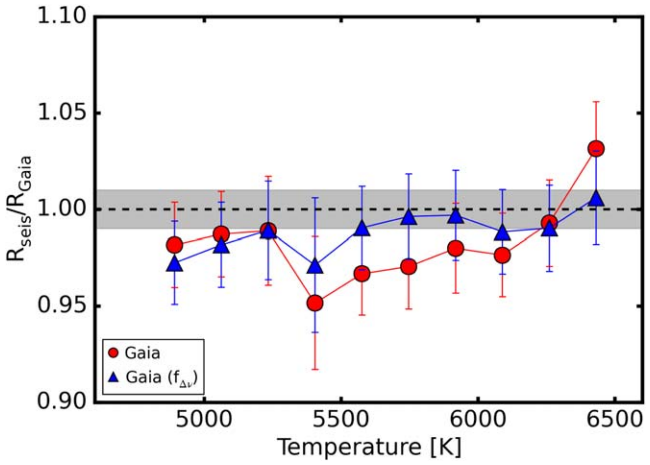

Figure 10. Comparison of asteroseismic radii derived from scaling relations with those derived from *Gaia* parallaxes, as a function of temperature. Red circles and blue triangles show our dwarf/subgiant sample without and with the use of $f_{\Delta\nu}$. Error bars indicate scatter in the median. The gray band indicates agreement to within 1%.

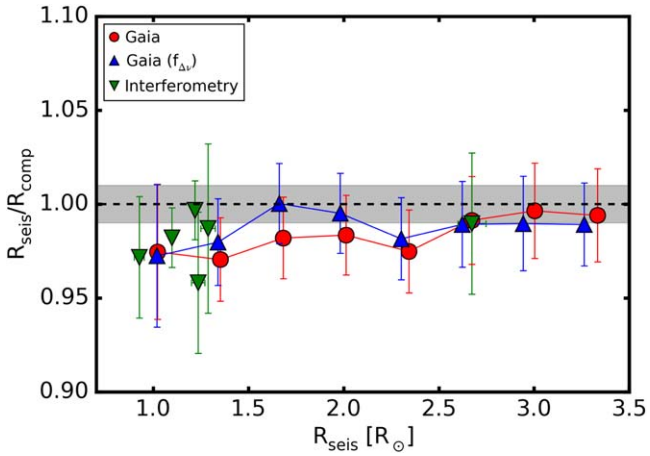

Figure 11. Comparison of asteroseismic radii derived from scaling relations with radii derived from three methods in the dwarf/subgiant radius regime ($R < 3.5\,R_\odot$). Red circles and blue upward triangles show our dwarf/subgiant sample without and with $f_{\Delta\nu}$. We also show stars with interferometrically measured radii (green triangles, Huber et al. 2012b; White et al. 2013; Johnson et al. 2014). Error bars indicate scatter in the median. The gray band indicates agreement to within 1%.

from this work. Hall et al. (2019) postulate that the difference they find between asteroseismic and *Gaia* absolute magnitudes could be explained by a systematic offset of −70 K in the spectroscopic temperature scale. Systematic differences among uncalibrated spectroscopic temperature scales can indeed disagree at this level. However, as we note in Section 3.3 the APOGEE temperature scale has a 1σ systematic uncertainty of 20 K because it has been calibrated to the IRFM temperature scale. Hall et al. (2019) also find that the choice of $f_{\Delta\nu}$ for red clump stars can significantly shift the red clump absolute magnitude scale. In this sense, an offset between the asteroseismic radius scale of red giants and red clump stars at the level of a few per cent is easily accommodated by the systematics in red clump models used to compute $f_{\Delta\nu}$ (e.g., Pinsonneault et al. 2018; An et al. 2019; Hall et al. 2019).

Sahlholdt & Silva Aguirre (2018) investigated the agreement between asteroseismology and *Gaia* radius scales among dwarfs and subgiants using *Gaia* DR2 parallaxes. Using scaling relations corrected according to White et al. (2013), they found a mean ratio of $\langle R_{\rm seis}/R_{Gaia}\rangle = 1.024 \pm 0.004$ (plotted in Figure 9). An additional set of asteroseismic scaling relation radii were computed using an additional set of surface corrections following Ball & Gizon (2014), which yielded a mean $\langle R_{\rm seis}/R_{Gaia}\rangle = 1.002 \pm 0.004$. Both of these estimates are mildly discrepant with our estimates and those of Huber et al. (2017) in the dwarf and subgiant regime. This could be due to the simple polynomial expansion in temperature that White et al. (2013) employ to parameterize $f_{\Delta\nu}$ as opposed to the grid-based interpolation scheme from BeSPP. The asteroseismic data from Sahlholdt & Silva Aguirre (2018) are also not calibrated to be on the cluster mass scale (as are the data we use in this work), which could help to explain the tension. Sahlholdt & Silva Aguirre (2018) also found deviations of ±3% at the extreme ends of their sample's temperature distribution, near 5400 and 6600 K (their Figure 4(c)). When we view our dwarf radius comparison as a function of temperature, shown in Figure 10, we see a similar effect at ∼5400 K, but not at higher temperatures. We believe that the lack of any trends beyond the 1% level with temperature at higher temperatures is a result of a difference in our adopted $f_{\Delta\nu}$.

Finally, Figure 9 also shows the mean and error on the mean of the radius agreement from Huber et al. (2017), who worked with *Gaia* DR1 and the same dwarf/subgiant asteroseismic sample used in this work. These results are consistent with ours, though with a larger uncertainty due to the less precise parallaxes in *Gaia* DR1.

To analyze our dwarf/subgiant radius comparison in more detail, we reproduce Figure 10 of Huber et al. (2017) in Figure 11 by comparing the *Gaia* results to independent comparisons from interferometry (e.g., Huber et al. 2012b; White et al. 2013). The ≈5% offset for subgiants identified by Huber et al. (2017) (with asteroseismic radii being smaller) is significantly reduced, suggesting that at least part of that offset may have been caused by an incomplete understanding of the *Gaia* parallax systematics in DR1, which would have affected the typically more distant subgiants more than the typically more nearby dwarfs. The largest offsets with *Gaia* DR2 are at the ≈2% level, fully consistent to within 1σ with the uncertainties for seismic radii derived from scaling relations using corrected $\Delta\nu$ values via $f_{\Delta\nu}$. This excellent agreement strongly suggests that scaling relation radii (using $f_{\Delta\nu}$ according to Equation (3)) are precise and accurate at the 2% ± 2% (syst.) level for stars in the range $R \approx 0.8$–$3.5\,R_\odot$.

Comparing *Kepler* first-ascent red giant branch and red clump asteroseismic parallaxes to Gaia DR2 parallaxes, Khan et al. (2019) find agreement between the Gaia and asteroseismic radius scales within ∼5%. We note that our results are not directly comparable because they do not account for $f_{\delta\nu}$, and so their level of agreement between *Gaia* and asteroseismic radius scales is an upper bound. Their results nevertheless confirm our conclusion that the asteroseismic radius scale is very accurate for red giants.

5.1.2. Constraints from Eclipsing Binaries

The largest study of the asteroseismic radius and mass scales of red giants using eclipsing binaries concluded that the radius scale was overestimated by 5% compared to the dynamical radius scale (Gaulme et al. 2016). The latter study examined stars with radii less than $15\,R_\odot$, and so our results for the stars of smaller radius ($R \leqslant 10\,R_\odot$) are directly comparable. Our results in this radius regime indicate that the agreement, in fact, is much better

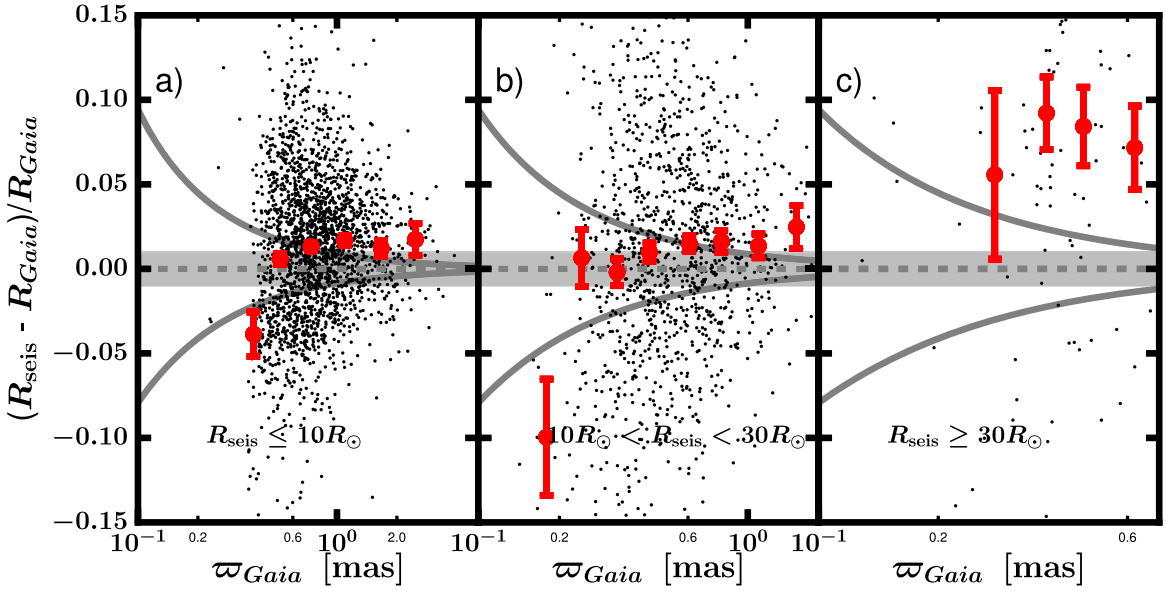

Figure 12. The fractional difference between asteroseismic and *Gaia* scales as a function of *Gaia* parallax for stars with (a) $R_{\rm seis} \leqslant 10\,R_\odot$, (b) $10\,R_\odot < R_{\rm seis} < 30\,R_\odot$, and (c) $R_{\rm seis} \geqslant 30\,R_\odot$. A gray band corresponding to ± 0.01 has been added to guide the eye. The solid gray curves show the expected trend with parallax of the fractional radius agreement if our adopted *Gaia* zero-point were shifted by the systematic uncertainty on c of ± 8.6 μas from Zinn et al. (2019); the flatness of the gray curves at high parallax indicates that high-parallax stars are essentially unaffected by the *Gaia* parallax zero-point correction. We use a high-parallax ($\varpi > 1$ mas) subsample of giants for all but the largest radius regime, $R_{\rm seis} \geqslant 30\,R_\odot$, to infer the radius agreement between asteroseismic and *Gaia* scales in this work.

than 5%. In that sense, our results accord with indications from Brogaard et al. (2018) that the temperatures in Gaulme et al. (2016) could be affected by the blending of the binary systems, therefore biasing the asteroseismic radii. For our sample, however, we use spectroscopic temperatures, which are not sensitive to blending in the same way as photometric estimates are, and we have furthermore selected against binarity using the *Gaia* data quality cuts described in Section 2.2.

5.2. Dependence on the Luminosity and Temperature Scales

In converting asteroseismic radii to parallaxes according to Equation (4), the luminosity scale enters through a dependence on the bolometric flux and distance/parallax, and the temperature enters through the explicit temperature dependence as well as the dependence of the bolometric correction on temperature. In this section, we discuss checks we have performed to ensure that our adopted luminosity and temperature scales in this work do not bias the radius agreement beyond our systematic uncertainty estimates in Section 3.2.

The observed variations of a_2 and a_3 using different choices for bolometric correction and extinction are generally within our estimated systematic bolometric correction and extinction error of 1% (Section 4.1), when including the random errors quoted on a_2 and a_3. Interestingly, the agreement between SED and *Gaia* radii is closer to unity than the asteroseismic–*Gaia* radius comparison. We show in Appendix A that it is the SED bolometric fluxes that differ the most from the MIST K_s-band bolometric corrections among the independent bolometric flux scales we compare to. So whereas the SED bolometric flux scale differs from the one we adopt for our asteroseismic–*Gaia* radius comparison by ∼4%, a difference of ∼0.2 mag in the SED extinctions and those from Rodrigues et al. (2014) that we adopt for our asteroseismic radii compensates to bring the SED radius scale closer to the *Gaia* radius scale.

The other component of the luminosity scale involves the parallaxes. The parallax zero-point correction we apply consists of both color- and magnitude-dependent terms (d and e in Equation (6)) as well as a global zero-point correction, c, with values taken from Zinn et al. (2019). An argument could be made that the parallax zero-point correction, which is itself constrained by the asteroseismic data from Zinn et al. (2019), necessarily enforces agreement between the asteroseismic and *Gaia* radius scales. For reasonable values of the color and magnitude terms in the *Gaia* parallax zero-point correction in Equation (6), however, the asteroseismic radii remain consistent with the *Gaia* radii. Figure 4(b) shows a model without color and magnitude terms and without radius scale factors a_2, a_3, and a_4. It is, in this sense, a conservative estimate of the agreement between asteroseismic and *Gaia* radii. This simplified model is still in excellent agreement with the observed ratio of asteroseismic to *Gaia* radii, which indicates that the asteroseismic radius correction factors that have been inferred in this work are not determined by choice of color or magnitude terms in the *Gaia* parallax zero-point. Regarding the global term, $c = 52.8$ μas, we show in Zinn et al. (2019) that the global parallax correction behaves differently than an asteroseismic radius correction factor. In this work, we have been conservative in our approach by inferring radius correction factors using only high-parallax stars ($\varpi > 1$ mas), which are essentially unaffected by a *Gaia* parallax zero-point correction of ≈0.05 mas. Not only should high-parallax stars be unbiased indicators of the radius agreement, but their asteroseismic parallaxes are more sensitive to errors in the asteroseismic radius scale than low-parallax stars (Zinn et al. 2019), and therefore are doubly useful for fitting the radius correction factors (a_1–a_4 in Equation (5); see Section 3.6). Looking at the stars least affected by a *Gaia* parallax correction in this way, we found that absolute agreement between the asteroseismic radius scale and the *Gaia* radius scale is within 2% ± 2% (syst.) for stars with radii below $R = 30\,R_\odot$. We also examined the differential trends using the full giant sample, which includes stars with low parallax (Section 4.2). The flat trend with parallax of the radius agreement shown in Figure 12

demonstrates that even these low-parallax giants have unbiased *Gaia* radii following a zero-point correction to the *Gaia* parallax scale. If errors in the parallax offset existed at the ± 9 μas level (the systematic error on the global parallax offset from Zinn et al. (2019), which is included in our 2% systematic uncertainty in the radius agreement), they would manifest as trends denoted by the solid gray curves in Figure 12.

Regarding the effect of the temperature scale on our results, we quantified the systematic effect of global temperature shifts to be at the 1% level. We illustrate with Figures 5(a) and (c) how the radius agreement would change if the APOGEE temperature scale were smaller by 40 K (Figure 5(a)) and larger by 40 K (Figure 5(c)). These temperature variations would constitute a 2σ systematic error according to our systematic uncertainty budget from Section 3.3, and in this sense represent an extreme example of the effect of temperature systematics. In these panels, we have included the effect of a temperature shift on the bolometric correction, which tends to moderate the effect of temperature on the radius, such that the *Gaia* radius does not scale as strongly with temperature as Equation (4) implies.

We have also verified that systematics due to the choice of $f_{\Delta\nu}$ (which affects the asteroseismic radii according to Equation (1)) does not significantly impact our results by using the prescription from Sharma et al. (2016) instead of using our nominal BeSPP $f_{\Delta\nu}$ values.[13]

6. Conclusions

1. For radii between 0.8 $R_\odot$ and 30 $R_\odot$ we conclude that the asteroseismic radius scale and the *Gaia* radius scale agree within 2%, which is within systematic uncertainties. There appear to be differential trends as a function of radius in this agreement, which are statistically significant ($4\% \pm 0.6\%$).
2. Our results agree with those from Hall et al. (2019), who performed a comparison of the asteroseismic and *Gaia* red clump absolute luminosity. In that work, the asteroseismic radii of the red clump stars were found to be larger than those from *Gaia*, which could be corrected by adjusting the temperature scale by 70 K. Here, we find a similar level of radius inflation, but can only attribute 1% of our 2% total systematic uncertainty on the radius inflation to temperature effects, because of the 0.5% accuracy of the temperature calibration of the infrared flux method.
3. After correcting *Gaia* parallaxes and asteroseismic radii according to our best-fitting model, the largest stars in our sample, with $R > 30\,R_\odot$, have asteroseismic radii that are too large by $8.7\% \pm 0.9\%$ (rand.) $\pm$ 2.0% (syst.).
4. We quantify the spatial correlations of *Gaia* parallaxes for the *Kepler* field, but find that they are unimportant for our analysis. At scales of $0\overset{\circ}{.}05$, 1°, and 5°, a typical parallax systematic error floor given a statistical uncertainty on parallax of $\sigma_{\varpi_{Gaia}}$ would be $0.1\,\sigma_{\varpi_{Gaia}}$, $0.07\sigma_{\varpi_{Gaia}}$, and $0.016\sigma_{\varpi_{Gaia}}$, respectively.
5. By investigating systematics in our radii due to bolometric corrections, we find that reasonable choices of bolometric correction from the literature disagree at the 2% level, which suggests that a fundamental bolometric correction scale at the level of a few per cent is difficult to arrive at.
6. We find only marginal evidence for an asteroseismic radius inflation of $2\% \pm 2\%$ (rand.) $\pm$ 2% (syst.) and mass inflation of $6\% \pm 8\%$ (rand.) $\pm$ 7% (syst.) for low-metallicity stars, $[\mathrm{Fe/H}] < -1.0$. For more solar-like metallicities, there are also no significant metallicity-dependent radius anomalies, to within 0.5% per dex in metallicity for giants and 1.1% per dex for dwarfs/subgiants.

In light of the remarkable agreement between asteroseismology and a fundamental parallactic radius scale, the systematics in bolometric correction, extinction, and temperature that we have identified in this work will likely limit future work on constraining the asteroseismic radius scale. For this reason, we are currently investigating the origin of the seemingly inflated asteroseismic radii for the most evolved giants in our sample ($30\,R_\odot \leqslant R_{\rm seis} < 50\,R_\odot$), whose scaling relation radii disagree beyond our nominal systematics level of 2%. It is likely the case that additional systematics will be significant in this regime (e.g., $\nu_{\rm max}$ measurement errors). Nevertheless, we believe that accounting for non-adiabatic effects in pulsation models in evolved stars could help to explain the radius inflation we observe in this work, and are thus conducting a complementary theoretical approach to understand these observations.

M.H.P. and J.Z. acknowledge support from NASA grants 80NSSC18K0391 and NNX17AJ40G. D.H. acknowledges support by the National Science Foundation (AST-1717000). D.S. is the recipient of an Australian Research Council Future Fellowship (project number FT1400147). Parts of this research were conducted by the Australian Research Council Centre of Excellence for All Sky Astrophysics in 3 Dimensions (ASTRO 3D), through project number CE170100013. A.S. is partially supported by MICINN grant ESP2017-82674-R and Generalitat de Catalunya grant 2017-SGR-1131. This research was supported in part by the National Science Foundation under grant No. NSF PHY-1748958 and by the Heising–Simons Foundation.

This work has made use of data from the European Space Agency (ESA) mission *Gaia* (https://www.cosmos.esa.int/gaia), processed by the *Gaia* Data Processing and Analysis Consortium (DPAC, https://www.cosmos.esa.int/web/gaia/dpac/consortium). Funding for the DPAC has been provided by national institutions, in particular the institutions participating in the *Gaia* Multilateral Agreement.

This paper includes data collected by the *Kepler* mission. Funding for the *Kepler* mission is provided by the NASA Science Mission directorate.

This research was partially conducted during the Exostar19 program at the Kavli Institute for Theoretical Physics at UC Santa Barbara, which was supported in part by the National Science Foundation under grant No. NSF PHY-1748958.

Funding for the Sloan Digital Sky Survey IV has been provided by the Alfred P. Sloan Foundation, the U.S. Department of Energy Office of Science, and the Participating Institutions. SDSS-IV acknowledges support and resources from the Center for High-Performance Computing at the University of Utah. The SDSS website is www.sdss.org. SDSS-IV is managed by the Astrophysical Research Consortium for the Participating Institutions of the SDSS

[13] The code of Sharma et al. (2016) for computing $f_{\Delta\nu}$, `asfgrid` (Sharma & Stello 2016), is available at http://www.physics.usyd.edu.au/k2gap/Asfgrid/.

Collaboration including the Brazilian Participation Group, the Carnegie Institution for Science, Carnegie Mellon University, the Chilean Participation Group, the French Participation Group, Harvard-Smithsonian Center for Astrophysics, Instituto de Astrofísica de Canarias, The Johns Hopkins University, Kavli Institute for the Physics and Mathematics of the Universe (IPMU)/University of Tokyo, the Korean Participation Group, Lawrence Berkeley National Laboratory, Leibniz Institut für Astrophysik Potsdam (AIP), Max-Planck-Institut für Astronomie (MPIA Heidelberg), Max-Planck-Institut für Astrophysik (MPA Garching), Max-Planck-Institut für Extraterrestrische Physik (MPE), National Astronomical Observatories of China, New Mexico State University, New York University, University of Notre Dame, Observatário Nacional/MCTI, The Ohio State University, Pennsylvania State University, Shanghai Astronomical Observatory, United Kingdom Participation Group, Universidad Nacional Autónoma de México, University of Arizona, University of Colorado Boulder, University of Oxford, University of Portsmouth, University of Utah, University of Virginia, University of Washington, University of Wisconsin, Vanderbilt University, and Yale University.

Software: BeSPP (Serenelli et al. 2013, 2017), asfgrid (Sharma & Stello 2016), emcee (Foreman-Mackey et al. 2013), NumPy (van der Walt et al. 2011), pandas (McKinney 2010), Matplotlib (Hunter 2007), IPython (Pérez & Granger 2007).

Appendix A
Bolometric Correction and Extinction Systematics

Our adopted bolometric scale in this work is the MIST K_s-band bolometric correction, BC_{K_s}, and therefore the first test we performed was a self-consistency check of the MIST bolometric corrections for the giant sample. We started out by assuming extinction coefficients, A_λ/A_V, for SDSS optical bands, $\lambda = g$, r, i from An et al. (2009). We then derived a visual extinction, A_V, based on each SDSS-K_s color. This process of course depends on both the SDSS-band and K_s-band bolometric corrections, and is effectively a test of the consistency of the bolometric corrections. We compared these extinctions to a common scale: our adopted extinction scale from Rodrigues et al. (2014). We took the median differences between the SDSS-band MIST extinctions and the extinctions of Rodrigues et al. (2014) for the giant sample as an indication of the self-consistency of the MIST bolometric corrections. We found that the g-band, r-band, and i-band MIST extinctions agree with the extinctions of Rodrigues et al. (2014) to within $1.3\% \pm 0.3\%$, $3.2\% \pm 0.2\%$, and $0.4\% \pm 0.4\%$, where the systematic error due to the uncertainty in the extinction coefficients dominates over the random uncertainty on the median of the MIST extinctions for the giant sample. We conclude that the MIST bolometric corrections are consistent with each other to at least 3%.

Ultimately, the quantity that we would like to pin down is not the K_s-band bolometric correction, but rather the bolometric flux itself. This quantity of course depends on not only the bolometric correction, but also the adopted extinction. We have adopted an infrared-based bolometric flux because of the relative insensitivity to extinction. Using the bolometric correction, we de-extinct the 2MASS K_s photometry by converting our A_V from Rodrigues et al. (2014) into A_{K_s} by way of an infrared extinction coefficient, as mentioned in Section 2.2. We adopt a solar irradiance from Mamajek et al. (2015), $f_0 = 1.361 \times 10^6$ erg s^{-1} cm^{-2}, and assume an apparent bolometric magnitude of $m_{\rm cal} = -26.82$ (using the visual magnitude of the Sun, $V_\odot = -26.76$, and its visual bolometric correction, $BC_{V,\odot} = -0.06$; Torres 2010). The bolometric flux is then $f_{\rm bol} = f_0\, 10^{-0.4(K_s - m_{\rm cal} + BC - A_{K_s})}$. To test the accuracy of our MIST K_s bolometric flux scale, we have computed bolometric fluxes for comparison using several other approaches, which are described below.

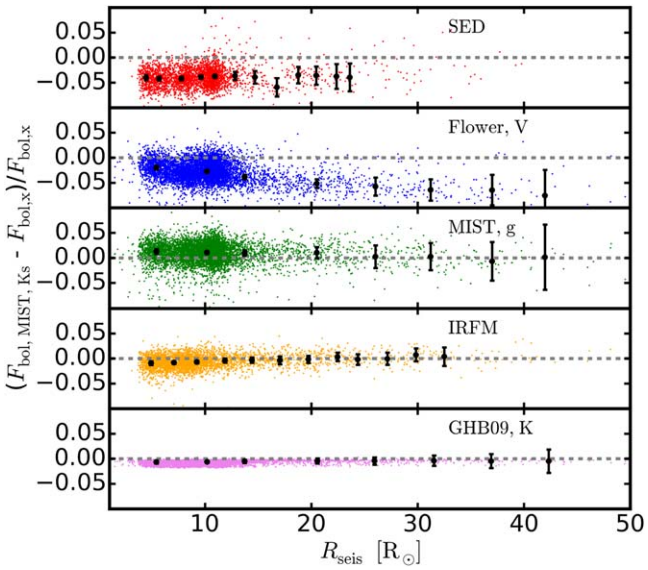

Figure 13. Fractional difference in our adopted K_s-band bolometric fluxes computed using MIST bolometric corrections and extinctions from Rodrigues et al. (2014) and various other bolometric flux systems, as a function of radius. See text for details.

First, we compare to a bolometric flux computed via SED fitting described in the main text. We computed the bolometric fluxes using this method for all giant stars with positive parallax and parallax errors less than 20%. The SED fitting was initialized with an initial guess for the extinction taken to be that of Rodrigues et al. (2014).

We also compare the bolometric fluxes we use to those from the IRFM method described in the main text. The IRFM hinges on a different dependence on temperature of the visual and infrared flux to iteratively estimate temperature and angular diameter (and bolometric flux). As the name implies, this method requires infrared photometry, for which we use J, H, and K_s from 2MASS. By way of visual photometry, we used g and r photometry from the *Kepler* Input Catalog (KIC; Brown et al. 2011), which has been recalibrated to be on the SDSS scale (Abolfathi et al. 2018) by Pinsonneault et al. (2012). As implemented in González Hernández & Bonifacio (2009), the IRFM requires V-band photometry, and so we transform g and r magnitudes to Johnson B and V according to Lupton (2005).[14] The extinctions in the de-extinction procedure are our adopted extinctions of Rodrigues et al. (2014).

The SED and IRFM bolometric fluxes are compared to our adopted K_s-band MIST bolometric fluxes in Figure 13. Also shown are three more sets of bolometric fluxes computed assuming the extinctions of Rodrigues et al. (2014): one using a g-band MIST bolometric correction, another the empirical visual bolometric correction from Flower (1996), and another

[14] https://www.sdss3.org/dr10/algorithms/sdssUBVRITransform.php

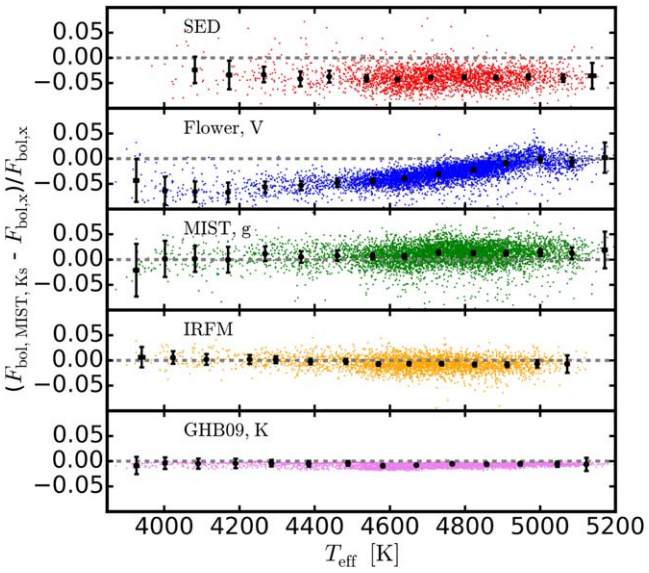

Figure 14. The same as Figure 13, except plotted as a function of temperature.

using the K_s-band bolometric correction from González Hernández & Bonifacio (2009) ("GHB09, K" in the figure).

The figure demonstrates first and foremost that the agreement across these methods is globally good. This is especially true when considering that the bolometric corrections span a range of two decades in publication date: from 1996 to present. In particular, this figure demonstrates excellent agreement in the mean fluxes ($0.73\% \pm 0.09\%$) between our adopted K_s-band MIST bolometric fluxes and the K_s-band bolometric fluxes using the bolometric correction from González Hernández & Bonifacio (2009). Part of this agreement is certainly due to the fact that any infrared flux scale is insensitive to the choice of extinction, but it more importantly establishes a consensus in the infrared bolometric corrections. Indeed, there is also excellent agreement with the IRFM bolometric flux scale ($0.66\% \pm 0.11\%$), even though that scale incorporates visual information (B and V) and therefore depends to some extent on the extinctions of Rodrigues et al. (2014).

The largest deviations in bolometric flux scale are between K_s MIST and SED (mean difference of $3.8\% \pm 0.1\%$) and between K_s MIST and V band ($3.0\% \pm 0.1\%$). As we see in Figure 14, the disagreement between our adopted infrared scale and the V-band scale is a strong function of temperature, which suggests there are genuine disagreements between the MIST models and the empirical V-band bolometric corrections. Unlike the other approaches, the SED approach does not assume the extinctions of Rodrigues et al. (2014). Differences in model atmospheres between those used in the C3K grid (C. Conroy et al. 2019, in preparation) and those used in the SED approach described in Stassun & Torres (2016) and Stassun et al. (2017) would result in different extinctions and bolometric corrections, both of which would affect bolometric flux agreement. On the extinction side, the predicted extinctions using the SED approach differ by ∼0.2 mag from those of Rodrigues et al. (2014). If adopting the bolometric fluxes from Rodrigues et al. (2014) and not allowing extinction as a free parameter in the SED fitting process, the SED bolometric fluxes would shift to be about 3% *lower* than our adopted K_s-band bolometric fluxes (otherwise, they are about 4% *higher* than the infrared fluxes). Shifts in extinction estimates from the SED fitting approach, in other words, map to shifts in bolometric fluxes. Given the relative insensitivity of the infrared bolometric fluxes to the choice of extinction, there are likely model color differences among Rodrigues et al. (2014), Stassun & Torres (2016), and C3K that would explain both (1) the different extinctions from the SED approach of Stassun & Torres (2016) and from that of Rodrigues et al. (2014) and (2) the remaining 3% difference between the SED and the MIST K_s-band bolometric fluxes when fixing the SED extinctions to those from Rodrigues et al. (2014).

The bolometric corrections we have discussed here reflect substantive differences in approach, as well as choice in adopted atmosphere models. For these reasons, we interpret these differences in the bolometric flux scale as 2σ systematics. So while, on the face of it, the largest mean offset in the bolometric corrections is ∼4%, we adopt this as a 2% systematic at the 1σ level. This choice for the systematic uncertainty in the bolometric correction scale for our work reflects the understanding, for instance, that the underlying atmosphere models for these two bolometric corrections (C3K and SED) are separated by 26 yr, and have significant departures in, e.g., adopted line lists. Ultimately, the largest differences we note in bolometric flux (∼2%–4%) map to differences of 1%–2% in radius space, as Table 1 indicates.

Appendix B
Spatial Correlations in DR2 Parallaxes

Having corrected for global, color-, and magnitude-dependent terms in the zero-point in *Gaia* parallaxes, we need to similarly account for the spatial dependence in the zero-point. The effect of spatial correlations in parallax can inflate the random error on inferred quantities in our sample, and so we describe here how we go about quantifying the off-diagonal elements in the covariance matrix, C.

Zinn et al. (2019) quantified the spatial dependence of the offset between parallaxes derived from asteroseismology (calculated according to Equation (4)) and those from *Gaia* DR1. The basis of the inference of spatially correlated systematics was a Pearson correlation coefficient that described the autocorrelation of the quantity $\varpi_{Gaia} - \varpi_{\rm seis}$ as a function of angular separation on the sky. This correlation function would be positive when two regions of the sky separated by an angular distance $\Delta\theta$ had *Gaia* parallax measurements that were both too low or both too high compared to the asteroseismic parallax, indicating a positive correlation at a certain angular scale. A negative angular correlation would exist where two patches of sky had *Gaia* parallaxes that were offset from the asteroseismic parallaxes in opposite directions. Where the two parallaxes agreed, the quantity would be zero.

We compute the binned Pearson correlation coefficient, correcting the *Gaia* parallaxes according to the zero-point model from Zinn et al. (2019) using the full giant sample, and then also remove any residual median in the difference in parallax scales. (If we were not to correct the *Gaia* parallaxes for global, magnitude-, and color-dependent errors before fitting for the spatial correlations, we would find too high a spatial parallax correlation due to the global offset between asteroseismic and *Gaia* parallaxes across the entire *Kepler* field.)

Table 3
The Best-fitting Parameters for Equation (9)

A	$\theta_{1/2}$	B	χ^2/dof
$4.031 \times 10^{-2} \pm 5.796 \times 10^{-5}$	$8\overset{\circ}{.}3 \pm 2\overset{\circ}{.}3$	$-3.497 \times 10^{-2} \pm 5.604 \times 10^{-5}$	7.930

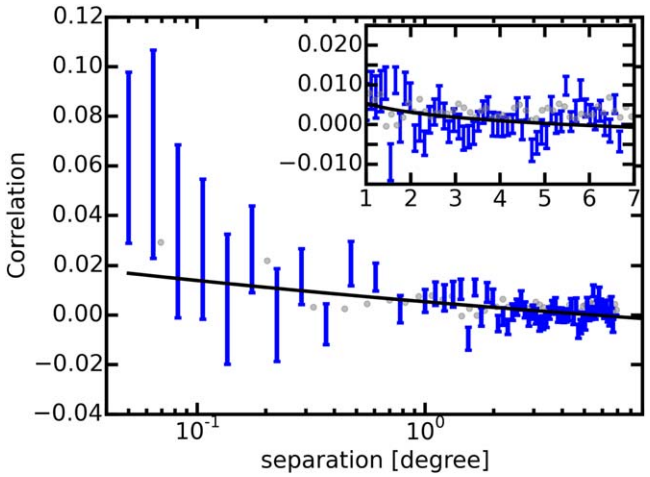

Figure 15. Error bars show the binned Pearson correlation coefficient of the asteroseismic–*Gaia* parallax difference as a function of angular separation. The black curve shows the fit using Equation (9). The points are spatial covariance points from the bottom panel of Figure 14 in Lindegren et al. (2018), rescaled to be a binned correlation coefficient by assuming a typical error for their quasar sample of 0.25 mas.

We fit the correlation coefficient of the parallax difference as a function of angular separation on the sky, $\Delta\theta$, with the following model:

$$\chi(\Delta\theta) = H(\Delta\theta)[A \exp(-\ln 2 \ln \Delta\theta/\theta_{1/2}) + B] \quad (9)$$

where A is a characteristic amplitude of the correlations, $\theta_{1/2}$ is a characteristic angular scale, and B is a constant. The Heaviside function, $H(\Delta\theta)$, ensures that the correlation is set to zero for the same star, $\chi(\Delta\theta = 0) = 0$. We follow the approach described in Zinn et al. (2019) to fit this functional form to the binned Pearson correlation coefficient. In this approach, the correlations between adjacent bins in the Pearson correlation coefficient (error bars in Figure 15) are taken into account, and the model is fitted using the MCMC method. We do not take into account edge effects as Zinn et al. (2019) do by fitting to simulated data. The best-fitting parameters for Equation (9) and their 1σ uncertainties are given in Table 3.

The observed correlation coefficient for our sample, along with the best-fitting model from Equation (9), is shown in Figure 15. We use this model for the angular parallax correlation, $\chi(\Delta\theta)$, in our covariance matrix when taking into account spatial correlations in parallax (Equation (8)). According to this best-fitting model, the level of correlation at angular separations of $0\overset{\circ}{.}05$ is 0.02, and it decreases to 0.01 at 1°, and to 0.0003 at 5°. This means that one cannot reduce the parallax uncertainty when averaging over more than 60, 200, or 4000 stars at these angular separations.

We find that our covariance agrees well with the covariance reported by Lindegren et al. (2018, hereafter L18) under a simple rescaling, assuming the median error of their quasar sample is 0.25 mas. We show the resulting data points from L18's Figure 14 in our Figure 15. The exponential behavior at $\Delta\theta \lesssim 0\overset{\circ}{.}1$ is similar to ours, and both our and L18's measurements indicate the presence of small-amplitude oscillatory behavior.

Whether or not we include the full covariance matrix in our analysis, according to Equations (7) and (8), our results are unaffected (compare "K MIST no cov" and "K MIST" entries in Table 1). This can be understood from the fact that the variability in the *Gaia* parallax scale as a function of position averages out over the *Kepler* field of view, leaving unaffected the central values of our radius agreement fit. Moreover, the relatively small number of stars in this high-parallax subsample means that one does not average down by $1/\sqrt{N}$ to the systematic floor set by the spatial correlations.

ORCID iDs

Joel C. Zinn https://orcid.org/0000-0002-7550-7151
Marc H. Pinsonneault https://orcid.org/0000-0002-7549-7766
Daniel Huber https://orcid.org/0000-0001-8832-4488
Dennis Stello https://orcid.org/0000-0002-4879-3519
Keivan Stassun https://orcid.org/0000-0002-3481-9052

References

Abolfathi, B., Aguado, D. S., Aguilar, G., et al. 2018, ApJS, 235, 42
Alonso, A., Arribas, S., & Martinez-Roger, C. 1994, A&A, 282, 684
Alonso, A., Arribas, S., & Martínez-Roger, C. 1999, A&AS, 139, 335
An, D., Pinsonneault, M. H., Masseron, T., et al. 2009, ApJ, 700, 523
An, D., Pinsonneault, M. H., Terndrup, D. M., & Chung, C. 2019, ApJ, 879, 81
Arribas, S., & Martinez Roger, C. 1987, A&A, 178, 106
Bailer-Jones, C. A. L., Rybizki, J., Fouesneau, M., Mantelet, G., & Andrae, R. 2018, AJ, 156, 58
Ball, W. H., & Gizon, L. 2014, A&A, 568, A123
Bertelli, G., Bressan, A., Chiosi, C., Fagotto, F., & Nasi, E. 1994, A&AS, 106, 275
Blackwell, D. E., Petford, A. D., & Shallis, M. J. 1980, A&A, 82, 249
Blackwell, D. E., & Shallis, M. J. 1977, MNRAS, 180, 177
Borucki, W., Koch, D., Basri, G., et al. 2008, in IAU Symp. 249, Exoplanets: Detection, Formation and Dynamics, ed. Y.-S. Sun, S. Ferraz-Mello, & J.-L. Zhou (Cambridge: Cambridge Univ. Press), 17
Bovy, J., Rix, H.-W., Green, G. M., Schlafly, E. F., & Finkbeiner, D. P. 2016, ApJ, 818, 130
Brogaard, K., Hansen, C. J., Miglio, A., et al. 2018, MNRAS, 476, 3729
Brown, T. M., Gilliland, R. L., Noyes, R. W., & Ramsey, L. W. 1991, ApJ, 368, 599
Brown, T. M., Latham, D. W., Everett, M. E., & Esquerdo, G. A. 2011, AJ, 142, 112
Casagrande, L., Ramírez, I., Meléndez, J., Bessell, M., & Asplund, M. 2010, A&A, 512, A54
Chaplin, W. J., Elsworth, Y., Davies, G. R., et al. 2014, MNRAS, 445, 946
Chaplin, W. J., Kjeldsen, H., Christensen-Dalsgaard, J., et al. 2011, Sci, 332, 213
Choi, J., Dotter, A., Conroy, C., et al. 2016, ApJ, 823, 102
Christensen-Dalsgaard, J. 1993, in ASP Conf. Ser. 42, GONG 1992. Seismic Investigation of the Sun and Stars, ed. T. M. Brown (San Francisco, CA: ASP), 347
Dotter, A. 2016, ApJS, 222, 8
Epstein, C. R., Elsworth, Y. P., Johnson, J. A., et al. 2014, ApJL, 785, L28
Fitzpatrick, E. L. 1999, PASP, 111, 63
Flower, P. J. 1996, ApJ, 469, 355
Foreman-Mackey, D., Hogg, D. W., Lang, D., & Goodman, J. 2013, PASP, 125, 306

Frandsen, S., Lehmann, H., Hekker, S., et al. 2013, A&A, 556, A138
Gaia Collaboration, Brown, A. G. A., Vallenari, A., et al. 2018, A&A, 616, A1
Gaia Collaboration, Prusti, T., de Bruijne, J. H. J., et al. 2016, A&A, 595, A1
Gaulme, P., McKeever, J., Jackiewicz, J., et al. 2016, ApJ, 832, 121
González Hernández, J. I., & Bonifacio, P. 2009, A&A, 497, 497
Green, G. M., Schlafly, E. F., Finkbeiner, D. P., et al. 2015, ApJ, 810, 25
Guggenberger, E., Hekker, S., Basu, S., & Bellinger, E. 2016, MNRAS, 460, 4277
Gunn, J. E., Siegmund, W. A., Mannery, E. J., et al. 2006, AJ, 131, 2332
Hall, O. J., Davies, G. R., Elsworth, Y. P., et al. 2019, MNRAS, 486, 3569
Holtzman, J. A., Hasselquist, S., Shetrone, M., et al. 2018, AJ, 156, 125
Holtzman, J. A., Shetrone, M., Johnson, J. A., et al. 2015, AJ, 150, 148
Huber, D., Chaplin, W. J., Christensen-Dalsgaard, J., et al. 2013, ApJ, 767, 127
Huber, D., Ireland, M. J., Bedding, T. R., et al. 2012a, ApJ, 760, 32
Huber, D., Ireland, M. J., Bedding, T. R., et al. 2012b, MNRAS, 423, L16
Huber, D., Stello, D., Bedding, T. R., et al. 2009, CoAst, 160, 74
Huber, D., Zinn, J., Bojsen-Hansen, M., et al. 2017, ApJ, 844, 102
Hunter, J. D. 2007, CSE, 9, 90
Johnson, J. A., Huber, D., Boyajian, T., et al. 2014, ApJ, 794, 15
Khan, S., Miglio, A., Mosser, B., et al. 2019, A&A, 628, A35
Kjeldsen, H., & Bedding, T. R. 1995, A&A, 293, 87
Kurucz, R. L. 1970, SAOSR, 309
Kurucz, R. L. 1993, in ASP Conf. Ser. 44, IAU Colloq. 138: Peculiar versus Normal Phenomena in A-type and Related Stars, ed. M. M. Dworetsky, F. Castelli, & R. Faraggiana (San Francisco, CA: ASP), 87
Lindegren, L., Hernández, J., Bombrun, A., et al. 2018, A&A, 616, A2
Majewski, S. R., Wilson, J. C., Hearty, F., Schiavon, R. R., & Skrutskie, M. F. 2010, in IAU Symp. 265, Chemical Abundances in the Universe: Connecting First Stars to Planets, ed. K. Cunha, M. Spite, & B. Barbuy (Cambridge: Cambridge Univ. Press), 480
Mamajek, E. E., Prsa, A., Torres, G., et al. 2015, arXiv:1510.07674
Mathur, S., Huber, D., Batalha, N. M., et al. 2017, ApJS, 229, 30
McKinney, W. 2010, in Proc. 9th Python in Science Conf., ed. S. van der Walt & J. Millman, 51
Michalik, D., Lindegren, L., & Hobbs, D. 2015, A&A, 574, A115
Mosser, B., Dziembowski, W. A., Belkacem, K., et al. 2013, A&A, 559, A137
Paxton, B., Bildsten, L., Dotter, A., et al. 2011, ApJS, 192, 3
Paxton, B., Cantiello, M., Arras, P., et al. 2013, ApJS, 208, 4
Paxton, B., Marchant, P., Schwab, J., et al. 2015, ApJS, 220, 15
Pérez, F., & Granger, B. E. 2007, CSE, 9, 21
Pinsonneault, M. H., An, D., Molenda-Żakowicz, J., et al. 2012, ApJS, 199, 30
Pinsonneault, M. H., Elsworth, Y., Epstein, C., et al. 2014, ApJS, 215, 19
Pinsonneault, M. H., Elsworth, Y. P., Tayar, J., et al. 2018, ApJS, 239, 32
Rawls, M. L., Gaulme, P., McKeever, J., et al. 2016, ApJ, 818, 108
Rodrigues, T. S., Girardi, L., Miglio, A., et al. 2014, MNRAS, 445, 2758
Sahlholdt, C. L., & Silva Aguirre, V. 2018, MNRAS, 481, L125
Salaris, M., Chieffi, A., & Straniero, O. 1993, ApJ, 414, 580
Schlafly, E. F., & Finkbeiner, D. P. 2011, ApJ, 737, 103
Schlegel, D. J., Finkbeiner, D. P., & Davis, M. 1998, ApJ, 500, 525
Serenelli, A., Johnson, J., Huber, D., et al. 2017, ApJS, 233, 23
Serenelli, A. M., Bergemann, M., Ruchti, G., & Casagrande, L. 2013, MNRAS, 429, 3645
Sharma, S., & Stello, D. 2016, Asfgrid: Asteroseismic Parameters for a Star v0.0.5, Astrophysics Source Code Library, ascl:1603.009
Sharma, S., Stello, D., Bland-Hawthorn, J., Huber, D., & Bedding, T. R. 2016, ApJ, 822, 15
Silva Aguirre, V., Casagrande, L., Basu, S., et al. 2012, ApJ, 757, 99
Skrutskie, M. F., Cutri, R. M., Stiening, R., et al. 2006, AJ, 131, 1163
Stassun, K. G., Collins, K. A., & Gaudi, B. S. 2017, AJ, 153, 136
Stassun, K. G., & Torres, G. 2016, AJ, 152, 180
Stello, D., Compton, D. L., Bedding, T. R., et al. 2014, ApJL, 788, L10
Tassoul, M. 1980, ApJS, 43, 469
Torres, G. 2010, AJ, 140, 1158
van der Walt, S., Colbert, S. C., & Varoquaux, G. 2011, CSE, 13, 22
van Leeuwen, F. 2007, A&A, 474, 653
Viani, L. S., Basu, S., Chaplin, W. J., Davies, G. R., & Elsworth, Y. 2017, ApJ, 843, 11
White, T. R., Bedding, T. R., Stello, D., et al. 2011, ApJ, 743, 161
White, T. R., Huber, D., Maestro, V., et al. 2013, MNRAS, 433, 1262
Yu, J., Huber, D., Bedding, T. R., et al. 2018, ApJS, 236, 42
Zinn, J. C., Huber, D., Pinsonneault, M. H., & Stello, D. 2017, ApJ, 844, 166
Zinn, J. C., Pinsonneault, M. H., Huber, D., & Stello, D. 2019, ApJ, 878, 136